Journal of Non-Newtonian Fluid Mechanics 285 (2020) 104338

Contents lists available at ScienceDirect

Journal of Non-Newtonian Fluid Mechanics

journal homepage: www.elsevier.com/locate/jnnfm

An Oldroyd-B solver for vanishingly small values of the viscosity ratio: Application to unsteady free surface flows

C. Viezel [a], M.F. Tomé [a,*], F.T. Pinho [b], S. McKee [c]

[a] Department of Applied Mathematics and Statistics, University of São Paulo, 13560-970, São Carlos, São Paulo, Brazil
[b] CEFT, Department of Mechanical Engineering, Faculty of Engineering, University of Porto, Rua Dr. Roberto Frias s/n, 4200-465, Porto, Portugal
[c] Department of Mathematics and Statistics, University of Strathclyde, 26 Richmond Street, G11XH, Glasgow, U.K.

ARTICLE INFO

Keywords:
Oldroyd-B model
EVSS
Free surface
Finite difference
Drop impact
Bouncing drop

ABSTRACT

This work is concerned with time-dependent axisymmetric free surface flows of Oldroyd-B fluids for any value of β, the ratio of solvent to total viscosities. The Oldroyd-B constitutive equation is dealt with by employing a novel technique to calculate the conformation tensor while an EVSS transformation allows the solution of the momentum equations coupled with the free surface stress conditions: this avoids numerical instabilities that can arise when using small values of β. The convergence of this new methodology is verified on pipe flow and also by comparing results from the literature for the time-dependent impacting drop problem. This approach is then used to predict the time-dependent free surface flow after a viscoelastic drop impacts a solid surface for β values in the range $[0, 1]$. The impacting drop problem is investigated for polymer solutions containing a small solvent contribution ($\beta \to 0$) or without any solvent viscosity ($\beta = 0$). In addition, a study of the bouncing drop problem for different values of β, Weissenberg and Reynolds numbers is undertaken.

1. Introduction

The importance of non-Newtonian free surface flows in industrial processes has attracted the attention of many scientists. Examples of such applications include polymer processing in the plastics industry such as mould filling of complex cavities. Such flows can be modelled by a system of nonlinear equations, but the presence of (multiple) moving free surfaces can make their solution challenging. Furthermore, for a particular polymer, it is not always obvious what the correct constitutive equation should be. One choice that must be made is between differential and integral constitutive models, or indeed a mixture of both. A large number of differential constitutive models have been developed over the past decades: Upper Convected-Maxwell (**UCM**) [1], Oldroyd-B [2], Phan-Thien-Tanner (PTT) [3], Giesekus [4], Extended Pom-Pom (Pom-Pom) [6,7], among others. On the other hand, integral constitutive models have been developed and studied by Papanastasiou et al. [8], Kaye [9] and Luo and Mitsoulis [10], amongst others. Integral constitutive equations require more sophisticated approaches to solve the governing equations numerically and require more computational resources and, possibly for these reasons, there has been a greater focus on differential constitutive models. In particular, the **UCM** and Oldroyd-B models have been extensively studied, employing finite element, finite volume and finite difference methods (e.g. [11–16,23–30]). Due to their unbounded elastic normal stresses, these models are arguably the most challenging viscoelastic constitutive equations from a numerical point of view (see e.g. [33,34]).

A decoupling strategy to calculate velocity and pressure has found favour. For instance, Hirt and Nichols [35] introduced the volume of fluid (VOF) method in the early 1980s: this has been used to simulate non-Newtonian flows by many investigators (e.g. [15,32,36–39]). This method, while easy to implement, suffers from numerical diffusion; to overcome this drawback several improved versions have been developed [36,38,40].

Another approach is to represent the free surface by a level set function which is convected with the fluid flow; its evolution in time is obtained through the solution of a hyperbolic equation. Osher and Sethian [41] are usually credited with introducing the idea and it has the capability of capturing multiphase flow phenomena. It has been used to simulate filament stretching and jet buckling [29,42,43], mould filling [44] and many other interesting applications (see e.g. [44–49]). A third approach is the front tracking method: unlike VOF or the level set method the front tracking method employs massless markers to describe the fluid interface. In two dimensions the interface between two fluids is described by a set of points (x_i, y_i) - *the markers* - while in three dimensions it is represented by a set of quadrilaterals and/or triangles. The coordinates of the markers are updated at each time step according to the velocity at the new time step. In two dimensions the interface is visualized by connecting these points by straight lines (i.e. zero or-

* Corresponding author.
E-mail addresses: murilo@icmc.usp.br (M.F. Tomé), fpinho@fe.up.pt (F.T. Pinho), sean.mckee@strath.ac.uk (S. McKee).

https://doi.org/10.1016/j.jnnfm.2020.104338
Received 7 February 2020; Received in revised form 20 June 2020; Accepted 24 June 2020
Available online 28 June 2020

der splines), while in three dimensions the interface is constructed from piece-wise linear surfaces described by quadrilaterals or triangles. The first ideas of this method were presented by Harlow and Welch [50], who introduced the Marker-and-Cell method in the early 1960s. Since its introduction, other improved versions have been developed and employed by many authors to simulate free surface flows of both Newtonian and non-Newtonian fluids in two and three dimensions (see, e.g. [16,50–60]).

In this paper we are concerned with axisymmetric viscoelastic free surface flows: the Oldroyd-B model is to be solved by an Eulerian finite difference method. The elastic-viscous-stress-splitting (EVSS) technique, introduced by Rajagopalan et al. [18] (see also [19–21]), has proved to be efficient for solving confined flows. The present work employs this stress splitting technique to solve the governing equations while the fluid free surface is handled by the front tracking technique specifically developed by Tomé et al. [16,17] for solving time-dependent free surface flows. A novel feature of our approach is that the extra-stress tensor is combined with the conformation tensor: the conformation tensor is then approximated by implicit finite differences in such a way that the resulting system of equations can be solved exactly. The stress splitting technique introduces a non-Newtonian tensor that is used on the free surface stress boundary conditions instead of the polymer stress tensor. This eliminates numerical instabilities if the flows were highly elastic and the solvent viscosity ratios $\beta = \frac{\eta_S}{\eta_0} = \frac{\lambda_2}{\lambda_1}$ were consequently small (for $\beta = 0$ there is even a singularity). Here, η_S and η_0 denote, respectively, solvent and total viscosities while λ_1, λ_2 are the relaxation and retardation times, respectively.

The application of both the EVSS transformation and the solution of the conformation tensor have allowed us to simulate free surface flows with vanishingly small values of the viscosity ratio β. This new methodology is in part verified by solving fully developed pipe flow and by a number of mesh refinement studies. The effectiveness of the technique is then demonstrated by solving the time-dependent impacting drop problem for very small values of the viscosity ratio β. A comparison with existing results in the literature is also made. New simulations of both drop spreading and drop bouncing are then presented and in particular, the bouncing of a drop is studied for various values of the Reynolds number, the viscosity ratio and the Weissenberg number.

2. Governing equations

The mass conservation and momentum equations are the basic equations for incompressible flows and can be written as,

$$\nabla \cdot \mathbf{v} = 0, \tag{1}$$

$$\rho\left[\frac{\partial \mathbf{v}}{\partial t} + \nabla \cdot (\mathbf{vv})\right] = -\nabla p + \nabla \cdot \boldsymbol{\tau} + \rho \mathbf{g}, \tag{2}$$

where $\mathbf{v}$ is the velocity vector, p is the scalar pressure, $\mathbf{g}$ is the gravity vector, ρ is the density of the fluid and $\boldsymbol{\tau}$ is the extra-stress tensor.

We are interested in flows governed by the Oldroyd-B rheological constitutive equation, that is defined by the following equation

$$\boldsymbol{\tau} + \lambda_1 \overset{\nabla}{\boldsymbol{\tau}} = 2\eta_0 \left[\mathbf{D} + \lambda_2 \overset{\nabla}{\mathbf{D}}\right], \quad \mathbf{D} = \frac{1}{2}\left[(\nabla \mathbf{v}) + (\nabla \mathbf{v})^T\right] \tag{3}$$

where $\mathbf{D}$ is the rate-of-deformation tensor, λ_1 is the relaxation time, λ_2 is the retardation time and η_0 is the total viscosity of the fluid. The upper-convected derivative of the stress tensor, denoted by the symbol $\overset{\nabla}{\boldsymbol{\tau}}$, is given by

$$\overset{\nabla}{\boldsymbol{\tau}} = \frac{\partial \boldsymbol{\tau}}{\partial t} + \nabla \cdot (\mathbf{v}\boldsymbol{\tau}) - \left(\nabla \mathbf{v}\right)^T \boldsymbol{\tau} - \boldsymbol{\tau}\left(\nabla \mathbf{v}\right).$$

This constitutive equation is usually solved under the rheological splitting

$$\boldsymbol{\tau} = \boldsymbol{\tau}_P + 2\beta\eta_0 \mathbf{D}, \tag{4}$$

where the second term on the right-hand side accounts for the Newtonian solvent stress contribution, and the polymer stress tensor $\boldsymbol{\tau}_P$ is calculated from the **UCM** equation

$$\boldsymbol{\tau}_P + \lambda_1 \overset{\nabla}{\boldsymbol{\tau}}_P = 2(1-\beta)\eta_0 \mathbf{D}, \tag{5}$$

and $\eta_0 = \eta_P + \eta_S$ is the sum of the solvent (η_S) and polymeric (η_P) viscosities. The coefficient $\beta = \frac{\eta_S}{\eta_0} = \frac{\lambda_2}{\lambda_1}$ measures the ratio between the solvent and the total viscosity of the fluid. The Oldroyd-B model can be derived from the kinetic theory of dilute polymer solutions and note that when $\eta_P \to 0, \lambda_1 \to 0$ (cf. Bird et al. [5])). When $\beta = 0$, Eq. (3) reduces to the *Upper-Convected Maxwell* (**UCM**) model and if $\beta = 1$ we have Newtonian flow since the relaxation time is also zero.

The extra-stress tensor $\boldsymbol{\tau}$ can be shown to be related to the conformation tensor $\mathbf{A}$ of the polymer additives, here represented by the mesoscopic model of dumb bells, by

$$\boldsymbol{\tau} = \frac{\eta_0}{\lambda_1}(1-\beta)(\mathbf{A} - \mathbf{I}) + 2\beta\eta_0 \mathbf{D}, \tag{6}$$

resulting in the time evolution equation

$$\mathbf{A} + \lambda_1 \overset{\nabla}{\mathbf{A}} = \mathbf{I}. \tag{7}$$

This equivalence is readily seen by substituting Eq. (6) into Eq. (3), and using the relationship between the relaxation and retardation times: $\lambda_2 = \beta\lambda_1$.

To solve the momentum equation Eq. (2), we employ the following transformation, known as EVSS [18] (see also [19–21])

$$\boldsymbol{\tau} = \mathbf{S} + 2\eta_0 \mathbf{D}, \tag{8}$$

where $\mathbf{S}$ is a non-Newtonian elastic stress tensor. After introducing this into the momentum equation Eq. (2), we obtain

$$\rho\left[\frac{\partial \mathbf{v}}{\partial t} + \nabla \cdot (\mathbf{vv})\right] = -\nabla p + \eta_0 \nabla^2 \mathbf{v} + \nabla \cdot \mathbf{S} + \rho \mathbf{g}. \tag{9}$$

The solutions ($\mathbf{v}$, p, $\boldsymbol{\tau}$) can therefore be obtained by solving the continuity Eq. (1) together with the momentum equation Eq. (9) using a projection method while the conformation tensor $\mathbf{A}$ can be calculated by solving Eq. (7). The extra-stress tensor $\boldsymbol{\tau}$ and the non-Newtonian stress tensor $\mathbf{S}$ are then computed from equations Eqs. (6) and (8), respectively.

However, in the literature, many works (e.g. [12,16,32]) dealing with the Oldroyd-B model make use of the rheological splitting Eq. (4) which, after being inserted into the momentum equation Eq. (2), leads to the transformed equation

$$\rho\left[\frac{\partial \mathbf{v}}{\partial t} + \nabla \cdot (\mathbf{vv})\right] = -\nabla p + \beta\,\eta_0 \nabla^2 \mathbf{v} + \nabla \cdot \boldsymbol{\tau}_P + \rho \mathbf{g}. \tag{10}$$

Note that this equation contains the term $\beta\eta_0\nabla^2\mathbf{v}$ instead of $\eta_0\nabla^2\mathbf{v}$ of Eq. (9).

2.1. Boundary conditions

The boundary conditions can be summarized as follows: on rigid boundaries the no-slip condition is imposed; on inflows, the velocity is prescribed while the extra-stress tensor obeys fully developed flow (details are given in Section 4). On outflows, homogeneous Neumann conditions are imposed; the free surface boundary conditions are discussed in the next section.

2.2. Free surface stress conditions

We consider unsteady axisymmetric free surface flows of a viscoelastic fluid flowing into a nonresistant atmosphere and assume negligible surface tension forces. This is a reasonable assumption since the fluids we shall consider are both very viscous and highly elastic. Under these conditions, the appropriate boundary conditions on the free surface of a viscous fluid are the vanishing of the normal and tangential stresses which can be stated as (see Batchelor [22])

$$\mathbf{n}^T \cdot (\boldsymbol{\sigma} \cdot \mathbf{n}) = 0, \tag{11a}$$

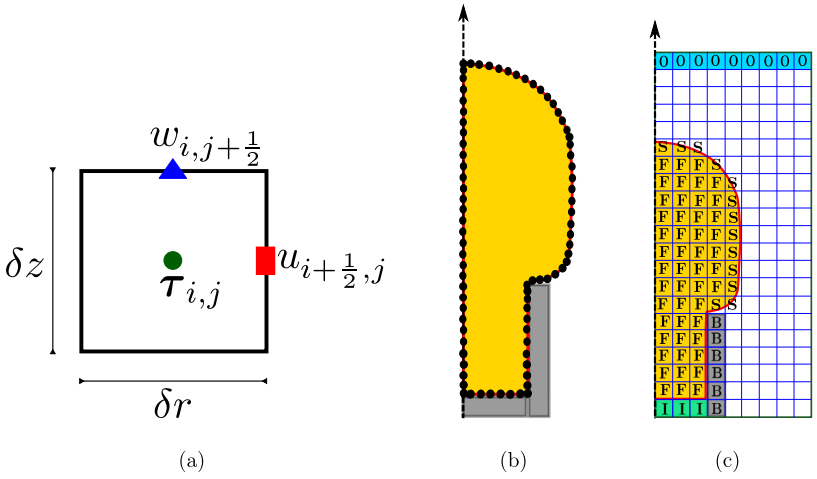

Fig. 1. (a) Description of a typical cell employed in the mesh, (b) Representation of fluid free surface (line connecting the particles) and volume of fluid (yellow area), (c) Type of cells in the domain.. (For interpretation of the references to color in this figure legend, the reader is referred to the web version of this article.)

$$\mathbf{m}^T \cdot (\boldsymbol{\sigma} \cdot \mathbf{n}) = 0, \tag{11b}$$

where $\boldsymbol{\sigma} = -p\mathbf{I} + \boldsymbol{\tau}$ is the total stress tensor, and, in two-dimensional axisymmetric flow, $\mathbf{n} = [n_r,\ n_z]^T$ and $\mathbf{m} = [n_z,\ -n_r]^T$ are the unit vectors, respectively, normal and tangential to the free surface.

By assuming axisymmetric flows and using cylindrical coordinates, and inserting the splitting defined by Eq. (4) into the free surface stress conditions Eqs. (11a,b) (for more details see [12,16,32]) gives rise to the following equations

$$p = \frac{2\beta}{\mathbf{Re}}\left[\frac{\partial u}{\partial r}n_r^2 + \left(\frac{\partial u}{\partial z} + \frac{\partial w}{\partial r}\right)n_r n_z + \frac{\partial w}{\partial z}n_z^2\right] + \tau_P^{rr}n_r^2 + 2\tau_P^{zr}n_r n_z + \tau_P^{zz}n_z^2, \tag{12a}$$

$$2\left(\frac{\partial w}{\partial z} - \frac{\partial u}{\partial r}\right)n_r n_z + \left(\frac{\partial u}{\partial z} + \frac{\partial w}{\partial r}\right)(n_r^2 - n_z^2) = \frac{\mathbf{Re}}{\beta}\left[(\tau_P^{rr} - \tau_P^{zz})n_r n_z + \tau_P^{rz}(n_z^2 - n_r^2)\right]. \tag{12b}$$

Equation Eq. (12a) is commonly used to compute the pressure on the free surface and poses no problem for any value of β while Eq. (12b) becomes singular as β approaches zero (**UCM** model). However, if β is small, numerical instabilities may appear especially if the flow is highly elastic or presents large stress gradients. Possibly for this reason, when using the rheological splitting (4), many investigators (e.g. [12,16,32]) have in the past solved free surface flows of Oldroyd-B fluids employing $\beta \geq 1/9$ in their calculations. A solution to this problem is developed next.

By introducing the EVSS transformation, Eq. (8), into the stress conditions Eqs. (11a,b), they can be written, in component form, as

$$p = \frac{2}{\mathbf{Re}}\left[\frac{\partial u}{\partial r}n_r^2 + \left(\frac{\partial u}{\partial z} + \frac{\partial w}{\partial r}\right)n_r n_z + \frac{\partial w}{\partial z}n_z^2\right] + S^{rr}n_r^2 + 2S^{zr}n_r n_z + S^{zz}n_z^2, \tag{13a}$$

$$2\left(\frac{\partial w}{\partial z} - \frac{\partial u}{\partial r}\right)n_r n_z + \left(\frac{\partial u}{\partial z} + \frac{\partial w}{\partial r}\right)(n_r^2 - n_z^2) = \mathbf{Re}\left[(S^{rr} - S^{zz})n_r n_z + S^{rz}(n_z^2 - n_r^2)\right]. \tag{13b}$$

Thus, by using the EVSS transformation we avoid the $1/\beta$ multiplier on the right hand side of Eq. (12b) and thereby the associated numerical instabilities when β is small. In this work we use Eqs. (13a) and (13b) instead of Eqs. (12a) and (12b).

3. Numerical method

The equations presented in Section 2 are solved by the finite difference method on a staggered grid (Fig. 1a displays the locations of the variables in a cell). The fluid is modelled by a front tracking method developed by Tomé et al. [17] wherein the fluid surface is described by a closed linear spline that is defined by markers (see Fig. 1b). To implement this technique, the cells within the mesh are divided into several types, as follows (see Fig. 1c):

- Rigid boundary (**B**): cells that define the location of rigid contours;
- Inflow boundary (**I**): cells that model 'fluid entrances' ('inflows');
- Outflow boundary (**O**): cells that define 'fluid exits' ('outflows');

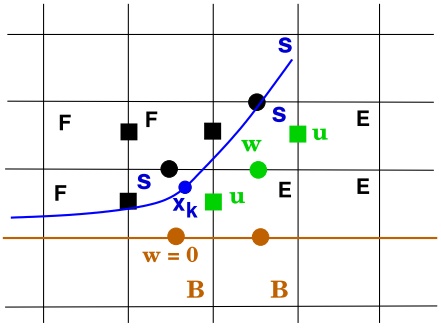

Fig. 2. Movement of the free surface (the blue curve) near a solid wall (the **brown** line); velocities shown by **brown** symbols are calculated by the no-slip condition while those represented by **green symbols** are computed from the free surface stress conditions (see Eq. (13b)) and the mass conservation equation. The velocities corresponding to the **black** symbols are obtained from the momentum equations. (For interpretation of the references to color in this figure legend, the reader is referred to the web version of this article.)

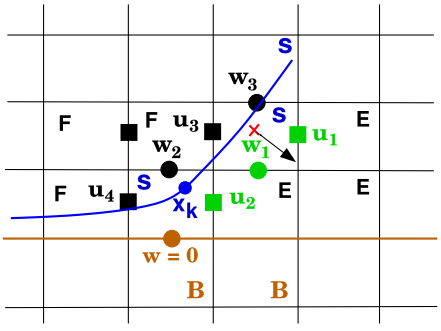

Fig. 3. Computation of the velocities on the free surface cells (the **green** velocities) and illustration of the application of the stress condition Eq. (13b). (For interpretation of the references to color in this figure legend, the reader is referred to the web version of this article.)

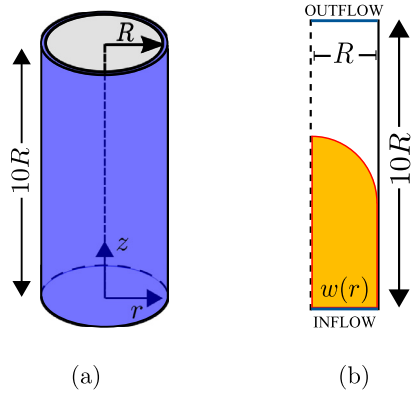

Fig. 4. Description of the flow domain (a) and computational domain (b).

▶ Empty cells (**E**): cells that do not contain fluid (see the white cells in Fig. 1c);

▶ Full cells (**F**): cells that contain fluid and have no contact with **E**-cell-faces;

▶ Surface cells (**S**): cells that contain fluid and have at least one face in contact with an **E**-cell-face.

3.1. Numerical algorithm

Eqs. (1) and (6) to (9), written in cylindrical coordinates, are solved for the unknowns $\mathbf{v}(r,z,t) = \left(u(r,z,t), w(r,z,t)\right)^T$, $p(r, z, t)$, $\boldsymbol{\tau}(r, z, t)$, $\mathbf{A}(r, z, t)$ and $\mathbf{S}(r, z, t)$, as follows. These equations are used in dimensionless form and contain the nondimensional numbers $\mathbf{Re} = \frac{\rho_0 U L}{\eta_0}$ (*Reynolds* number), $\mathbf{Wi} = \lambda_1 \frac{U}{L}$ (*Weissenberg* number) and $Fr = \frac{U}{\sqrt{L g}}$ (*Froude* number), in which L, U and ρ_0 are typical scales for length, velocity and mass (via density), respectively (for details see [16]). The calculational cycle is performed in three steps, as follows:

STEP 1: Calculation of $\mathbf{v}^{n+1} = \mathbf{v}(r,z,t_{n+1})$ and $p^{n+1} = p(r,z,t_{n+1})$

The algorithm for calculating $\mathbf{v}^{n+1}$ and p^{n+1} embodies some ideas from the technique presented by Tomé et al. [16]. The pressure field is uncoupled from the mass (Eq. (1)) and momentum (Eq. (9)) equations by using the projection method of Chorin [61].

Let δt be the time step used, $t_{n+1} = t_n + \delta t$, and let $\mathbf{v}^n = \mathbf{v}(r,z,t_n)$, $\boldsymbol{\tau}^n = \boldsymbol{\tau}(r,z,t_n)$, $\mathbf{D}^n$, $\mathbf{A}^n$ and $\mathbf{S}^n$ be known at time t_n.

A tentative velocity field $\tilde{\mathbf{v}}^{n+1}$ is then calculated by the implicit Euler method applied to the momentum equation by solving

$$\tilde{\mathbf{v}}^{n+1} - \frac{\delta t}{\mathbf{Re}}\nabla^2\tilde{\mathbf{v}}^{n+1} = \mathbf{v}^n + \delta t\left\{ -\nabla\cdot(\mathbf{vv})^n - \nabla p^n + \nabla\cdot\mathbf{S}^n + \frac{1}{Fr^2}\mathbf{g}\right\}. \quad (14)$$

This gives rise to a sparse linear system that is efficiently solved by the conjugate gradient method. It can be shown [62] that this velocity field contains the correct vorticity at time t but it does not conserve mass in general. Thus, a potential function $\psi(r,z,t_{n+1})$ is computed such that

$$\nabla^2\psi^{n+1} = \nabla\cdot\tilde{\mathbf{v}}^{n+1} \quad (15)$$

while the updated velocity field, $\mathbf{v}^{n+1}$, is calculated from

$$\mathbf{v}^{n+1} = \tilde{\mathbf{v}}^{n+1} - \nabla\psi^{n+1}. \quad (16)$$

Thus the velocity $\mathbf{v}^{n+1}$ ensures that mass is conserved while the vorticity remains unchanged.

In this work, we borrow some ideas from the implicit technique of Oishi et al. [63] that couples the boundary condition for the pressure on the free surface, given by Eq. (11a), and the mass conservation equation Eq. (1). This technique consists of applying the mass conservation equation together with the pressure condition on the free surface and the equation for the velocity $\mathbf{v}^{n+1}$, Eq. (16), on surface cells. By doing this, new equations for the potential function ψ^{n+1} are derived and added to the set of equations that originated from the application of the discrete version of the Poisson equation Eq. (15) in F-cells. In surface cells, these new equations contain terms like $\frac{\partial^2}{\partial r\partial z}$ which are first order approximated by finite differences. This results in the total linear system becoming non-symmetric and therefore it is solved by the bi-conjugate gradient method.

After obtaining ψ^{n+1}, the pressure is calculated using

$$p^{n+1} = p^n + \frac{\psi^{n+1}}{\delta t}. \quad (17)$$

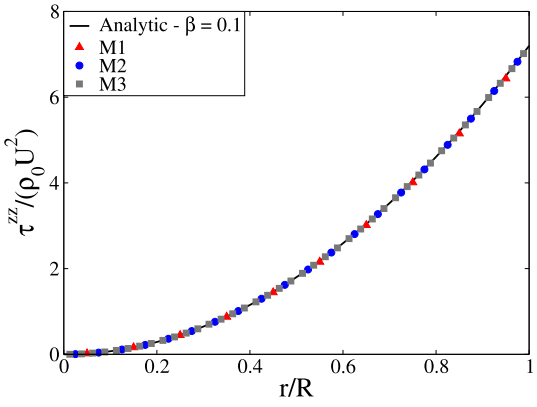

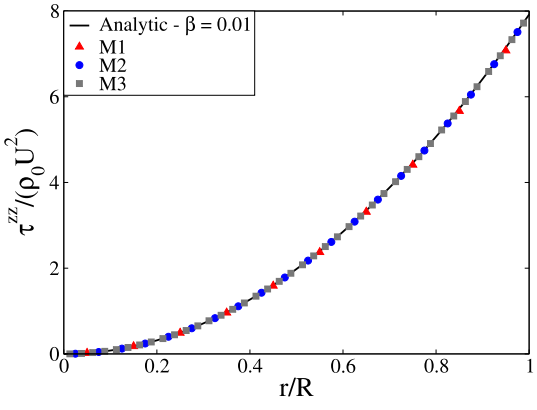

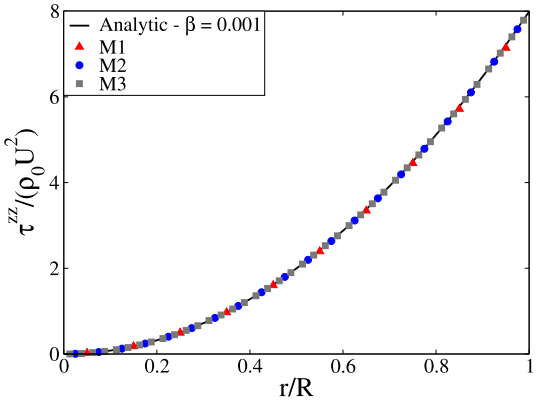

Fig. 5. Comparison of $\tau^{zz}(r)$ with the analytic solution for pipe flow. Results obtained with $\beta = 0.1, 0.01, 0.001$.

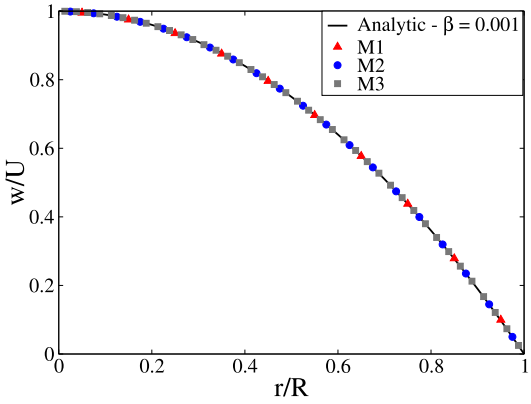

Fig. 6. Comparison of $w(r)$ with the analytic solutions for pipe flow. Results obtained with $\beta = 0.001$ on meshes M1, M2 and M3.

STEP 2: Calculation of $\mathbf{A}^{n+1} = \mathbf{A}(r, z, t_{n+1})$, $\boldsymbol{\tau}^{n+1} = \boldsymbol{\tau}(r, z, t_{n+1})$ and $\mathbf{S}^{n+1} = \mathbf{S}(r, z, t_{n+1})$

In this step we first compute the conformation tensor $\mathbf{A}^{n+1} = \mathbf{A}(r, z, t_{n+1})$ by solving Eq. (7) using finite differences as follows.

On each surface ($\mathbf{S}_{i,j}$) and full ($\mathbf{F}_{i,j}$) cells, Eq. (7) is implicitly approximated by the equation

$$\mathbf{A}^{n+1} + \delta t\left\{\frac{1}{\mathbf{Wi}}\mathbf{A}^{n+1} - (\nabla\mathbf{v}^{n+1})^T\mathbf{A}^{n+1} - \mathbf{A}^{n+1}(\nabla\mathbf{v}^{n+1})\right\} = \mathbf{A}^n + \delta t\left\{\frac{1}{\mathbf{Wi}}\mathbf{I} - \nabla\cdot(\mathbf{v}^{n+1}\mathbf{A}^n)\right\}, \tag{18}$$

resulting in the following (4 × 4)-linear system for the components of $\mathbf{A}^{n+1}$:

$$\begin{cases}
I. & [A^{rr}]^{n+1}_{i,j} + \delta t * \left\{\frac{1}{\mathbf{Wi}}[A^{rr}]^{n+1}_{i,j} - 2\left(\frac{\partial u}{\partial r}[A^{rr}] + \frac{\partial u}{\partial z}[A^{rz}]\right)^{n+1}_{i,j}\right\} = \\
 & [A^{rr}]^{n}_{i,j} + \delta t * \left\{\frac{1}{\mathbf{Wi}} - \frac{1}{r_i}\frac{\partial\left(ru^{n+1}[A^{rr}]^n\right)}{\partial r}\Big|_{i,j} - \frac{\partial\left(w^{n+1}[A^{rr}]^n\right)}{\partial z}\Big|_{i,j}\right\}; \\
II. & [A^{\theta\theta}]^{n+1}_{i,j} + \delta t * \left\{\frac{1}{\mathbf{Wi}}[A^{\theta\theta}]^{n+1}_{i,j} - 2\frac{u^{n+1}_{i,j}}{r_i}[A^{\theta\theta}]^{n+1}_{i,j}\right\} = \\
 & [A^{\theta\theta}]^{n}_{i,j} + \delta t * \left\{\frac{1}{\mathbf{Wi}} - \frac{1}{r_i}\frac{\partial\left(ru^{n+1}[A^{\theta\theta}]^n\right)}{\partial r}\Big|_{i,j} - \frac{\partial\left(w^{n+1}[A^{\theta\theta}]^n\right)}{\partial z}\Big|_{i,j}\right\}; \\
III. & [A^{zz}]^{n+1}_{i,j} + \delta t * \left\{\frac{1}{\mathbf{Wi}}[A^{zz}]^{n+1}_{i,j} - 2\left(\frac{\partial w}{\partial r}\right)^{n+1}_{i,j}[A^{rz}]^{n+1}_{i,j} - 2\left(\frac{\partial w}{\partial z}\right)^{n+1}_{i,j}[A^{zz}]^{n+1}_{i,j}\right\} = \\
 & [A^{zz}]^{n}_{i,j} + \delta t * \left\{\frac{1}{\mathbf{Wi}} - \frac{1}{r_i}\frac{\partial\left(ru^{n+1}[A^{zz}]^n\right)}{\partial r}\Big|_{i,j} - \frac{\partial\left(w^{n+1}[A^{zz}]^n\right)}{\partial z}\Big|_{i,j}\right\}; \\
IV. & [A^{rz}]^{n+1}_{i,j} + \delta t * \left\{\left(\frac{1}{\mathbf{Wi}} + \left(\frac{u}{r}\right)^{n+1}_{i,j}\right)[A^{rz}]^{n+1}_{i,j} - \left(\frac{\partial w}{\partial r}[A^{rr}] + \frac{\partial u}{\partial z}[A^{zz}]\right)^{n+1}_{i,j}\right\} = \\
 & [A^{rz}]^{n}_{i,j} + \delta t * \left\{-\frac{1}{r_i}\frac{\partial\left(ru^{n+1}[A^{rz}]^n\right)}{\partial r}\Big|_{i,j} - \frac{\partial\left(w^{n+1}[A^{rz}]^n\right)}{\partial z}\Big|_{i,j}\right\}.
\end{cases} \tag{19}$$

By writing this linear system in matrix form, it yields

$$\begin{bmatrix} a_{11} & 0 & 0 & a_{14} \\ 0 & a_{22} & 0 & 0 \\ 0 & 0 & a_{33} & a_{34} \\ a_{41} & 0 & a_{43} & a_{44} \end{bmatrix}\begin{bmatrix} A^{rr} \\ A^{\theta\theta} \\ A^{zz} \\ A^{rz} \end{bmatrix}^{n+1} = \begin{bmatrix} F_1 \\ F_2 \\ F_3 \\ F_4 \end{bmatrix}, \tag{20}$$

where the matrix coefficients are given by

$$\begin{cases}
a_{11} = 1.0 + \delta t\left(\frac{1}{\mathbf{Wi}} - 2\frac{\partial u^{n+1}}{\partial r}\right), \\
a_{22} = 1.0 + \delta t\left(\frac{1}{\mathbf{Wi}} - 2\frac{u^{n+1}}{r}\right), \quad a_{14} = -2\delta t\frac{\partial u^{n+1}}{\partial z}, \\
a_{33} = 1.0 + \delta t\left(\frac{1}{\mathbf{Wi}} - 2\frac{\partial w^{n+1}}{\partial z}\right), \quad a_{34} = -2\delta t\frac{\partial w^{n+1}}{\partial r}, \quad a_{41} = -\delta t\frac{\partial w^{n+1}}{\partial r}, \\
a_{44} = 1.0 + \delta t\left(\frac{1}{\mathbf{Wi}} + \frac{u^{n+1}}{r}\right), \quad a_{43} = -\delta t\frac{\partial u^{n+1}}{\partial z},
\end{cases} \tag{21}$$

$$\begin{cases}
F_1 = [A^{rr}]^n + \delta t\left[\frac{1}{\mathbf{Wi}} - \frac{1}{r}\frac{\partial(ru^{n+1}[A^{rr}]^n)}{\partial r} - \frac{\partial(w^{n+1}[A^{rr}]^n)}{\partial z}\right], \\
F_2 = [A^{\theta\theta}]^n + \delta t\left[\frac{1}{\mathbf{Wi}} - \frac{1}{r}\frac{\partial(ru^{n+1}[A^{\theta\theta}]^n)}{\partial r} - \frac{\partial(w^{n+1}[A^{\theta\theta}]^n)}{\partial z}\right], \\
F_3 = [A^{zz}]^n + \delta t\left[\frac{1}{\mathbf{Wi}} - \frac{1}{r}\frac{\partial(ru^{n+1}[A^{zz}]^n)}{\partial r} - \frac{\partial(w^{n+1}[A^{zz}]^n)}{\partial z}\right], \\
F_4 = [A^{rz}]^n + \delta t\left[\frac{1}{\mathbf{Wi}} - \frac{1}{r}\frac{\partial(ru^{n+1}[A^{rz}]^n)}{\partial r} - \frac{\partial(w^{n+1}[A^{rz}]^n)}{\partial z}\right].
\end{cases} \tag{22}$$

The derivatives in Eq. (21) are approximated by second order finite differences while the convective terms in Eq. (22) are calculated by employing the high order upwind method CUBISTA [64]. The solution of the linear system Eq. (20) is obtained exactly for 2D flow in the rz-plane and it is found to be

$$\begin{cases}
[A^{\theta\theta}]^{n+1} = \frac{F_2}{a_{22}}, \quad [A^{rz}]^{n+1} = \frac{F_4 - \frac{a_{41}}{a_{11}}F_1 - \frac{a_{43}}{a_{33}}F_3}{a_{44} - \frac{a_{41}}{a_{11}}a_{14} - \frac{a_{43}}{a_{33}}a_{34}}, \\
[A^{rr}]^{n+1} = \frac{1}{a_{11}}\left[F_1 - a_{14}[A^{rz}]^{n+1}\right], \quad [A^{zz}]^{n+1} = \frac{1}{a_{33}}\left[F_3 - a_{34}[A^{rz}]^{n+1}\right].
\end{cases} \tag{23}$$

Thus, the tensor $\boldsymbol{\tau}^{n+1}$ may now be calculated directly from

$$\boldsymbol{\tau}^{n+1} = \frac{1}{\mathbf{Re}\,\mathbf{Wi}}(1-\beta)(\mathbf{A}^{n+1} - \mathbf{I}) + \frac{2}{\mathbf{Re}}\beta\mathbf{D}^{n+1}, \tag{24}$$

and the non-Newtonian stress tensor $\mathbf{S}^{n+1}$ is computed from (after introducing $\boldsymbol{\tau}^{n+1}$ into Eq. (8))

$$\mathbf{S}^{n+1} = \frac{1}{\mathbf{Re}\,\mathbf{Wi}}(1-\beta)(\mathbf{A}^{n+1} - \mathbf{I}) + \frac{2}{\mathbf{Re}}(\beta - 1)\mathbf{D}^{n+1}. \tag{25}$$

STEP 3: Free surface movement

We employ a front tracking method in which the fluid free surface is made up of a set of markers $\mathbf{x_k} = \{(r_k, z_k)\}$ that define a linear spline curve where, here, the index k denotes a specific marker. Once the updated velocity $\mathbf{v}^{n+1}$ has been calculated, the positions of these markers are moved to new positions using local velocities $\mathbf{v_k}^{n+1} = (u_k, w_k)^{n+1}$ that are calculated by making bilinear interpolation involving the four nearest cell velocities. For instance, with regard to Fig. 2, the velocity u_k of the marker $\mathbf{x_k}$ is calculated using 3-black-squares (■) and 1-green-square (■) velocities while the velocity w_k is computed using 1-black-circle (●), 2-brown-circles (●) and 1-green-circle (●) velocities. The new positions of the markers $\{\mathbf{x_k}\}$ is then found by solving

$$\frac{d\,\mathbf{x_k}}{dt} = \mathbf{v_k}^{n+1}, \tag{26}$$

employing a 2nd-order R-K method. In our method, markers are not permitted to collide with solid walls where both velocities components at (r_k, z_k) would vanish. Notwithstanding, they are allowed to be as close as $(1/N)h$ where N is a given integer and h is the grid spacing. In this manner, the free surface (represented by the blue curve in Fig. 2) is assumed to be in contact with a solid wall when a marker is at a distance of $(1/N)h$ from it. This causes the normal velocity of the marker to become small ($u_n \approx 0$) while its tangential velocity can be large. The results presented in this work were obtained with $N = 8$.

To illustrate how to apply the free surface stress condition given by Eq. (13b), consider the velocities shown in green color in Fig. 3. The velocity $\mathbf{u_2}$ is computed directly from the mass conservation equation discretized at the centre (i, j) of the $\mathbf{S}$-cell that contains the marker $\mathbf{x_k}$, giving

$$\frac{1}{r_i}\left[\frac{r_{i+1/2}\mathbf{u_2} - r_{i-1/2}\mathbf{u_4}}{\delta r}\right] + \frac{\mathbf{w_2} - \mathbf{0}}{\delta z} = 0 \text{ which yields } \mathbf{u_2} = \left\{\frac{r_{i-1/2}}{r_{i+1/2}}\right\}\mathbf{u_4} - \left\{\frac{r_i}{r_{i+1/2}}\right\}\left(\frac{\delta r}{\delta z}\right)\mathbf{w_2}. \tag{27}$$

To calculate the velocities $\mathbf{u_1}$ and $\mathbf{w_1}$, we apply both the mass conservation equation and the free surface stress condition given by Eq. (13b) at

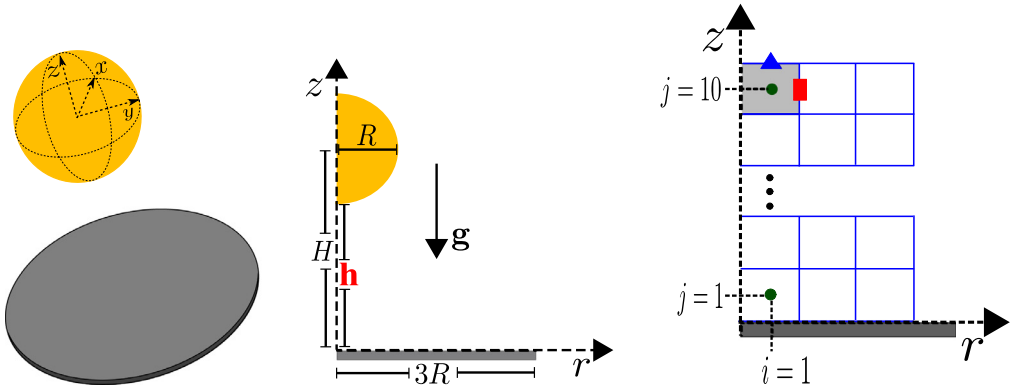

Fig. 7. Simulation of an impacting drop. (a) 3D view of initial state; (b) Computational domain employed; (c) Reference cell.

the centre (i, j) of the surface cell that has $\mathbf{u_1}$ and $\mathbf{w_1}$ on its faces (see Fig. 3). For this cell, the local normal vector is assumed to be at an angle of -45^0 between the coordinate axes (see the arrow in Fig. 3) so $\mathbf{n} = (\frac{\sqrt{2}}{2}, -\frac{\sqrt{2}}{2})$. Inserting this normal vector into Eq. (13b) and considering the mass conservation equation we obtain

$$\frac{\partial u}{\partial r} - \frac{\partial w}{\partial z} = \frac{\mathbf{Re}}{2}(S^{zz} - S^{rr}) \tag{28}$$

$$\frac{1}{r}\frac{\partial (ru)}{\partial r} + \frac{\partial w}{\partial z} = 0. \tag{29}$$

Now, discretizing these equations at the centre (i, j) of the of the **S**-cell yields

$$\frac{\mathbf{u_1} - \mathbf{u_3}}{\delta r} - \frac{\mathbf{w_3} - \mathbf{w_1}}{\delta z} = \frac{\mathbf{Re}}{2}\left(S^{zz}_{i,j} - S^{rr}_{i,j}\right) \tag{30}$$

$$\frac{1}{r_i}\left[\frac{r_{i+1/2}\mathbf{u_1} - r_{i-1/2}\mathbf{u_3}}{\delta r}\right] + \frac{\mathbf{w_3} - \mathbf{w_1}}{\delta z} = 0. \tag{31}$$

Eqs. (30) and (31) consist of a (2×2)-linear system for the unknowns $\mathbf{u_1}$ and $\mathbf{w_1}$ which has the solution

$$\mathbf{u_1} = \left[\frac{r_i + r_{i-1/2}}{r_i + r_{i+1/2}}\right]\mathbf{u_3} + 0.5\,\delta r \mathbf{Re}\left[\frac{r_i}{r_i + r_{i+1/2}}\right]\left(S^{zz}_{i,j} - S^{rr}_{i,j}\right), \tag{32}$$

$$\mathbf{w_1} = \mathbf{w_3} + \frac{\delta z}{\delta r}\frac{1}{r_i}\left[r_{i+1/2}\mathbf{u_1} - r_{i-1/2}\mathbf{u_3}\right]. \tag{33}$$

For other configurations of free surface cells, the calculation of the velocities (the green velocities) is similar to the cases worked out here. The work of Tomé et al. [23] presents details on how to define the normal vector for a general configuration of the free surface.

With this treatment, we have been able to simulate flows having moving free surfaces interacting with solid walls (see e.g. [17]) without the necessity of imposing a contact angle.

4. Verification and validation of results

To verify the numerical method described in Section 3, fully developed pipe flow was simulated and the results are displayed in Section 4.1. In addition, in Section 4.2, results from simulations of an unsteady free surface drop impacting on a solid wall are compared with other numerical results from the literature.

The results presented in this work were obtained using the following time step size (assuming $\delta r = \delta z$):

$\delta t = FACT * \delta r^2/4$, where $FACT = 0.1$.

Because the momentum equation was solved implicitly by the Euler method, this time step size is more restrictive than the CFL condition and therefore is enough to guarantee stable solutions for small Reynolds number flows.

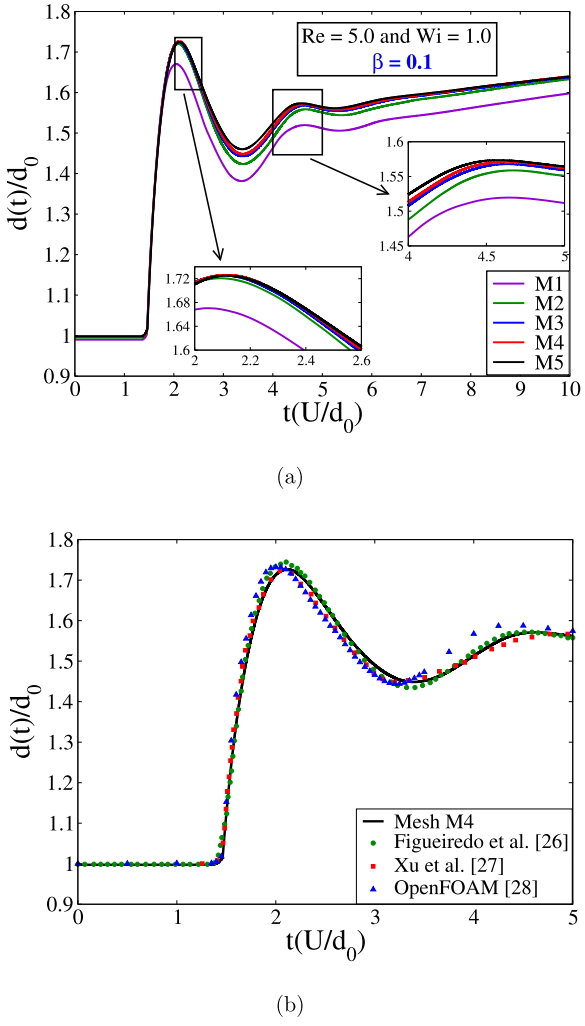

Fig. 8. Simulation of a drop impacting a disk with **Re** = 5, **Wi** = 1 and $\beta = 0.1$. (a) Mesh refinement; (b) Comparison with other investigators. Our results were obtained on mesh M4.

4.1. Steady laminar pipe flow

A pipe of radius $R = 1.0$ m and length $H = 10R$ m (see Fig. 4a) comprised the computational domain $\Omega = [0,\ R] \times [0,\ 10R]$ as illustrated in

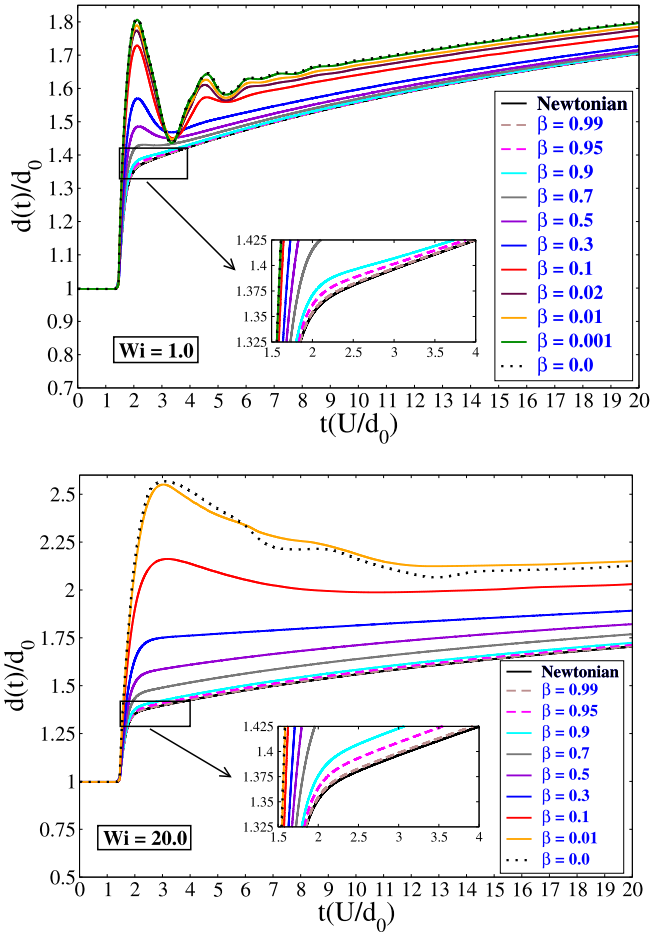

Fig. 9. Simulation of drop impacting a disk with **Re** = **5** and variation of β: (a) **Wi** = **1**, (b) **Wi** = **20**.

Fig. 4b. The pipe was empty initially and fluid was injected at the inflow by imposing the following fully developed profile:

$$w(r) = \left(1 - r^2\right), \quad u(r) = 0, \quad \dot{\gamma} = \frac{dw}{dr} = -2r,$$
$$\tau^{zz}(r) = \frac{2}{\mathbf{Re}}\mathbf{Wi}\left(1-\beta\right)\dot{\gamma}^2, \quad \tau^{rz}(r) = \frac{1}{\mathbf{Re}}\dot{\gamma}, \quad \tau^{rr}(r) = \tau^{\theta\theta}(r) = 0. \tag{34}$$

The input data were: $L = R = 1$ m, $U = 1$ ms^{-1}, $\rho = 1000$ kg m^{-3}, $\eta_0 = 1000$ Pa.s, $\lambda_1 = 1$ s, $\lambda_1 = 1$ s, $\lambda_2 = \beta\lambda_1$. Therefore, $\mathbf{Re} = \frac{\rho U L}{\eta_0} = 1$ and $\mathbf{Wi} = \lambda_1 \frac{U}{L} = 1$. The values of β used in these simulations are displayed in Table 1.

By using the meshes presented in Table 2, this problem was simulated until time $t(U/L) = 100$ on each mesh.

Table 1
Values of β used in the pipe flow.

β	0.1000	0.0100	0.0010	0.0000

Table 2
Meshes used to simulate pipe flow.

Mesh $\mathbf{M_K}$	**M1** (10 × 100)	**M2** (20 × 200)	**M3** (40 × 400)
$\delta_K = \delta_r = \delta_z$	0.1000	0.0500	0.0250
Cells in the mesh	(10 × 100)	(20 × 200)	(40 × 400)

Table 3
L_2-errors between analytic and numerical solutions calculated on meshes M1, M2 and M3.

(a) $\beta = 0.1$			
Mesh $\mathbf{M_K}$	$E(w(r, z_m))$	$E(\tau^{rz}(r, z_m))$	$E(\tau^{zz}(r, z_m))$
M1	1.6838e-03	5.7013e-03	3.1615e-02
M2	4.2603e-04	1.4370e-03	8.0048e-03
M3	1.0655e-04	3.6005e-04	2.0071e-03
(b) $\beta = 0.001$			
Mesh $\mathbf{M_K}$	$E(w(r, z_m))$	$E(\tau^{rz}(r, z_m))$	$E(\tau^{zz}(r, z_m))$
M1	1.6838e-03	5.7008e-03	3.5097e-02
M2	4.2603e-04	1.4364e-03	8.8842e-03
M3	1.0655e-04	3.6005e-04	2.2278e-03

Table 4
Calculated convergence order.

(a) $\beta = 0.1$			
Meshes used	w	τ^{rz}	τ^{zz}
M1-M2	1.9827	1.9882	1.9817
M2-M3	1.9994	1.9968	1.9957
(b) $\beta = 0.001$			
Meshes used	w	τ^{rz}	τ^{zz}
M1-M2	1.9798	1.9889	1.9821
M2-M3	1.9972	1.9957	1.9957

Fig. 5 displays the numerical solutions obtained for $\tau^{zz}(r, z_m)$ for $\beta = 0.1, 0.01, 0.001$ while Fig. 6 shows the solutions for $w(r, z_m)$ and $\tau^{rz}(r, z_m)$ using $\beta = 0.001$. These solutions were plotted at the middle of the pipe at $z_m = 5R$. For comparisons, the analytic solutions are also plotted. It can be seen that the numerical solutions agree well with the corresponding solutions on the different meshes. Moreover, Table 3 shows that the L_2-errors calculated with the norm defined by Eq. (35) decay as the mesh is refined and Table 4 displays that the calculated convergence order is about two. This is in accordance with the second-order finite difference approximations employed to solve the equations. The results obtained with $\beta = 0$ were very similar to those obtained with

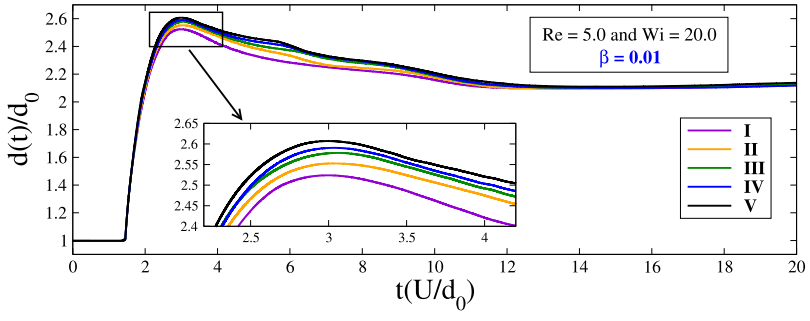

Fig. 10. Mesh refinement analysis for the case **Re** = **5**, **Wi** = **20** and $\beta = 0.01$. Meshes used: **I, II, III, IV** and **V** defined in Table 7.

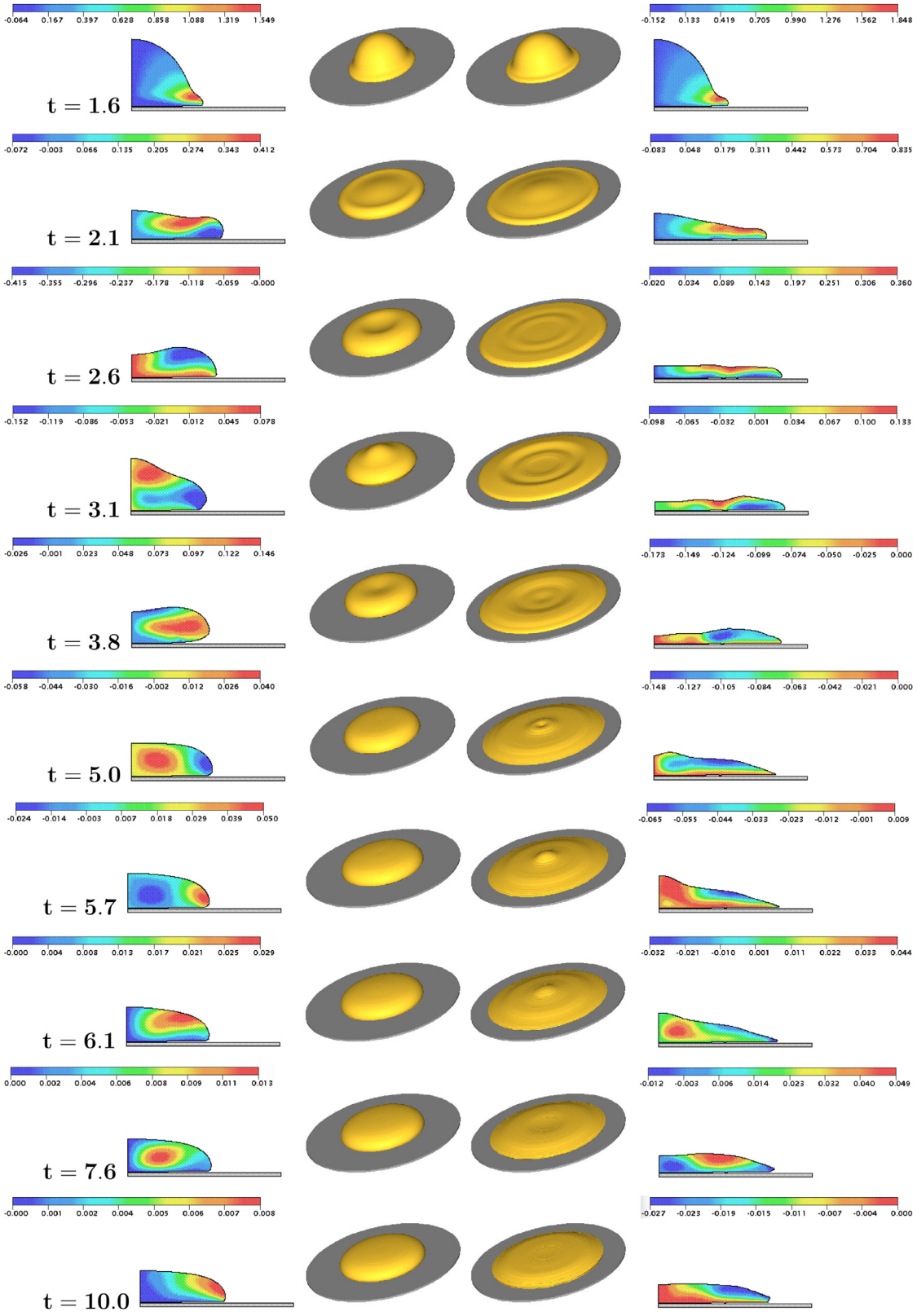

Fig. 11. Simulation of a drop spreading over a disk - **Re = 5**, $\beta = 0.01$ and **Wi = 1** and **20**, at selected times. Contour plots display the u-velocity. Left column: **Wi = 1**, right column: **Wi = 20**.

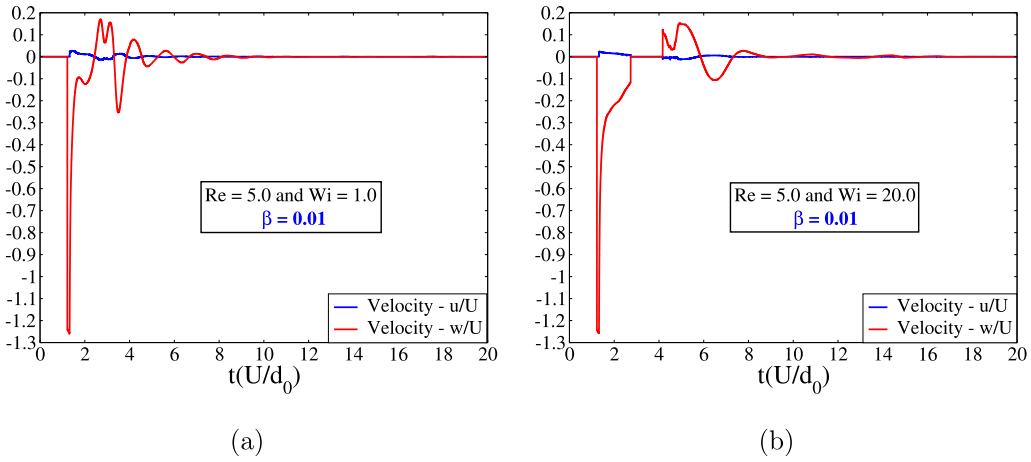

Fig. 12. Variation of the velocities $u(t)$ and $w(t)$ at the **cell(1,10)** identified in Fig. 7c. (a) **Wi = 1**; (b) **Wi = 20**. The discontinuity in the velocities is due to the fact that **cell(1,10)** became empty of fluid over the time interval **[2.78, 4.2]**.

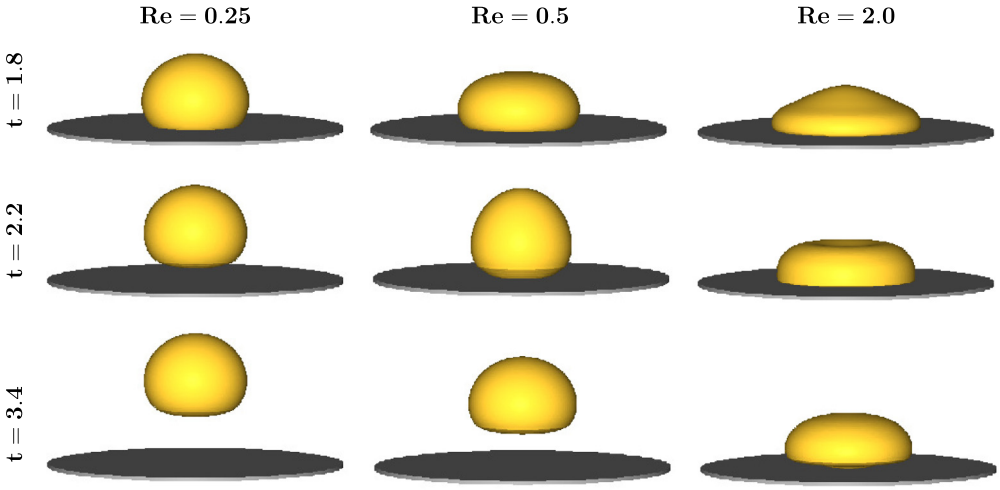

Fig. 13. Numerical simulation of drop rebound at selected times for **Wi = 1**, $\beta = 0.01$ and **several values of Re**.

$\beta = 0.001$ and were not displayed for conciseness.

$$E(\cdot)_K = \sqrt{\delta_K \sum_j \left[(\cdot)_{\text{Anal.}} - (\cdot)_{\text{Num.}}\right]^2}, \quad \times (\delta_K \text{ is the spacing of mesh } \mathbf{M_K} \text{ in Table 2}) \tag{35}$$

Note that this summation is across the pipe section at $z = 5R$.

4.2. Drop impacting: General features

To test the code on a time-dependent problem with a free surface flow, we simulated the flow of an axisymmetric drop (see Fig. 7a) modelled by an Oldroyd-B fluid. This is an appropriate problem to assess our numerical algorithm on time-dependent flows possessing large free surface deformations. It also allows us to effect a comparison with solutions obtained by other numerical techniques.

We considered an initially spherical drop of diameter $d_0 = 2R$ that was positioned above a circular disk at a height H (see Fig. 7b). At $\mathbf{t = 0}$, the drop starts to fall under gravity with initial velocity $w(r, z, 0) = -U$; the components of the extra-stress tensor $\boldsymbol{\tau}$ were initially assigned to be zero. After the drop hits the disk it is anticipated that it will flow radially increasing its diameter $d(t)$, but after a short period of time elastic forces should come into play and the velocities within the drop are expected to reverse causing it to start contracting with a consequent decrease in its diameter $d(t)$. We are interested in studying the effects of parameters **Wi** and β on variation with time of the drop diameter $d(t)$.

Table 5
Input data (SI units) used in the impacting drop simulation.

$d_0 = 2R[m]$	$H[m]$	$U[ms^{-1}]$	$\lambda_1[s]$	$\eta_0[Pa.s]$	$\rho\ [kg\ m^{-3}]$	Fr
0.02	0.04	1.0	0.02	4.0	1000.0	2.2576

As a check on our code, we performed mesh refinement followed by comparisons with numerical results from other investigators. The parameters associated with the flow used in these simulations are listed in Table 5 which give the following dimensionless numbers **Re = 5**, **Wi = 1**, $\beta = \mathbf{0.1}$. Simulations were carried out until time $t(U/d_0) = 10$ employing the meshes defined in Table 6. The results obtained are displayed in Fig. 8a where it can be seen that the solutions exhibit good mesh convergence. Moreover, Fig. 8b compares $d(t)$ with the results obtained by Figueiredo et al. [26], Xu et al. [27] and the OpenFOAM code [28]. It is clear that the time evolution of $d(t)$ obtained by our code agrees well with the results from the literature and provides us with some confidence that our code is behaving well on this particular unsteady free surface flow.

4.3. Simulation of impacting drop: Effects of Wi and β

To demonstrate the capability of this technique for solving time-dependent viscoelastic free surface flows, the input data displayed in

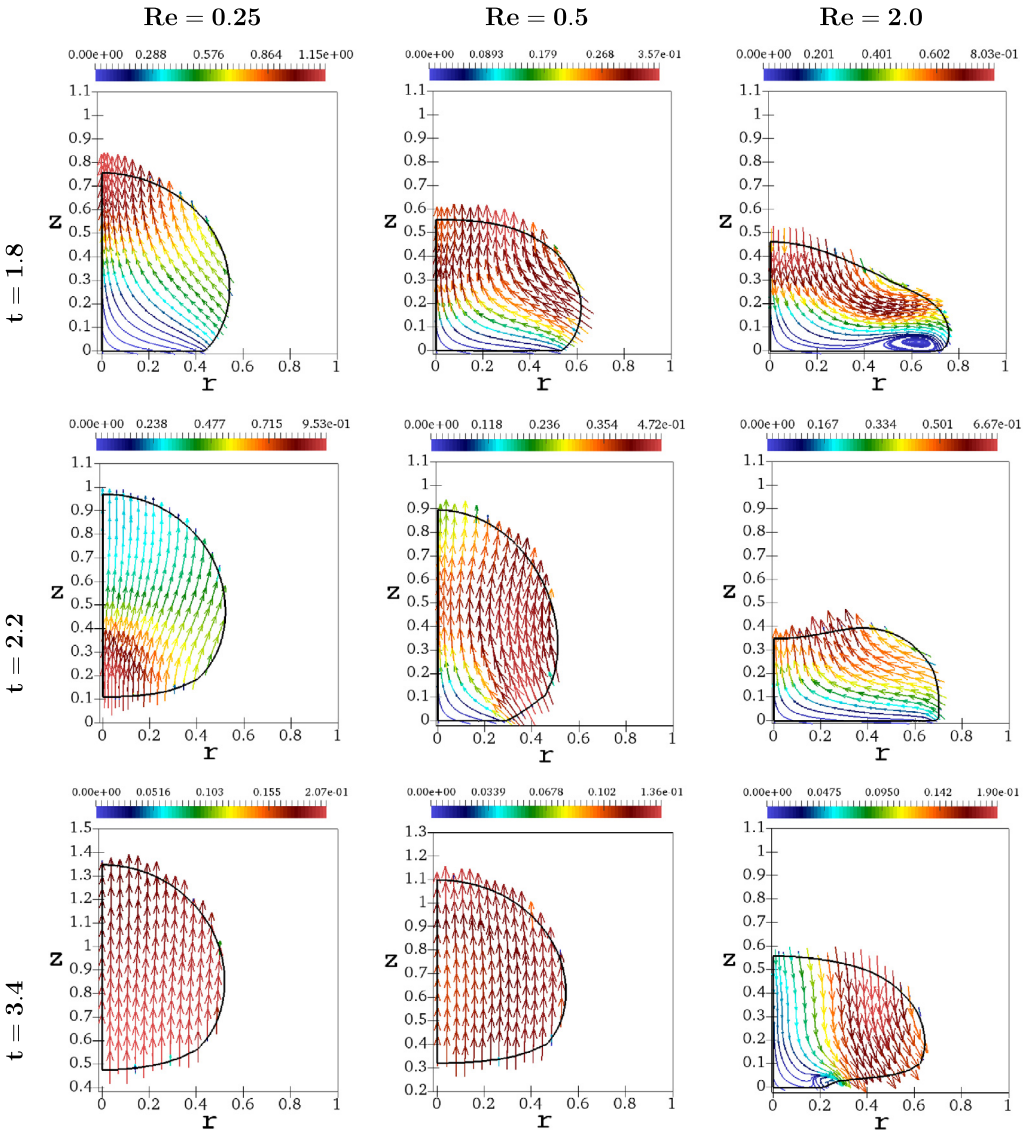

Fig. 14. Velocity field at selected times for **Wi = 1** and $\beta = 0.01$ and several Reynolds numbers.

Table 6
Meshes employed in the simulations of drop impacting.

Mesh	M1	M2	M3	M4	M5
spacing (δ_K/d_0)	0.050000	0.025000	0.016666	0.012500	0.006250

Table 5 and mesh M4 were employed to simulate the impacting drop problem for a range of values of β and **Wi**. In particular, the effect of β was extensively investigated in the range 0 to 1 and the flows near the two limits were carefully considered.

We started with the case **Re = 5** and **Wi = 1** and simulated the impacting drop for

$\beta = 0, 0.001, 0.01, 0.02, 0.1, 0.3, 0.5, 0.7, 0.9, 0.95, 0.99$. The Newtonian flow, corresponding to $\beta = 1$, was also simulated for reference. These simulations were performed until the nondimensional time $t(U/d_0) = 20$.

Fig. 9 a displays the time history of $d(t)$ for each value of β. It is readily seen that the results with $\beta = 0.9, 0.95, 0.99$ are similar, approaching the results of the Newtonian drop ($\beta = 1$) and showing that after the drop has impacted the disk, at time $t \approx 1.4$, it continued to flow radially, with $d(t)$ increasing monotonically. The results with $\beta = 0.3, 0.5, 0.7$ display a small radial expansion and radial contraction of the drop that occurred at times $t \approx 2.1$ and $t \approx 3.7$, respectively. It is seen that, after the initial contraction, the drop flowed radially outwards like the Newtonian drop. For $\beta = 0.001, 0.01, 0.02, 0.1$, the behaviour of $d(t)$ is more noticeable. The increase in polymer concentration within the drop, proportional to $1 - \beta$, provided greater elasticity to the fluid so that more of the fluid has a stress build-up and relaxation over a finite time, allowing the drop to expand and contract twice. The magnitude of these oscillations became more pronounced as the value of β decreased and for $\beta = 0.001$, the diameter $d(t)$ is about the same as that obtained with the **UCM** model ($\beta = 0$, see the black dotted curve in Fig. 9a) as we might have anticipated. The reason the low β fluids exhibit larger diameters immediatelly after impact is related to the finite time it takes for the resisting shear stresses from the polymer contribution to increase, whereas they appear instantly in the Newtonian solvent contribution. The simul-

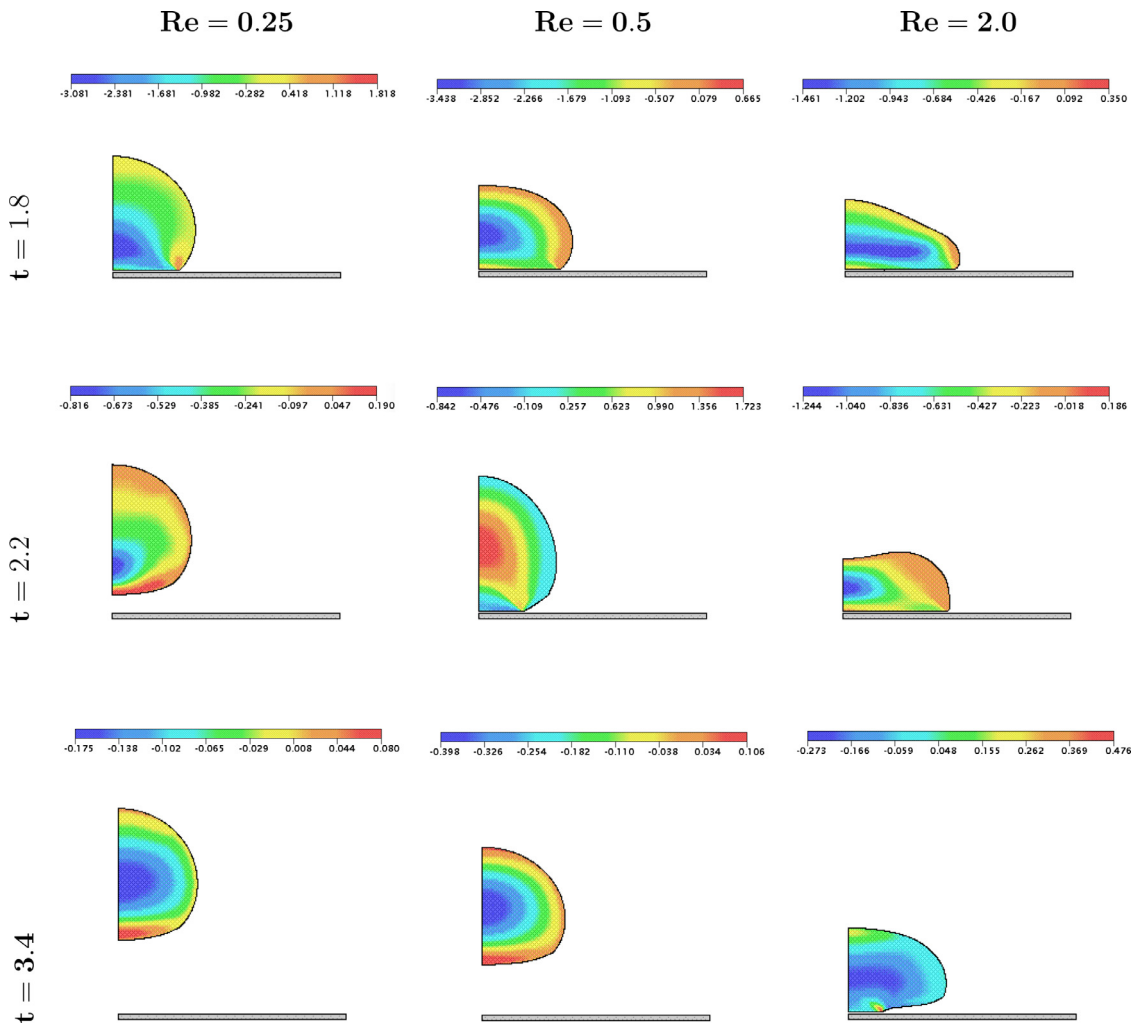

Fig. 15. First normal stress difference $N_1 = \tau^{zz} - \tau^{rr}$ for different Reynolds numbers at times $\mathbf{t} = \mathbf{1.8}, \mathbf{2.2}, \mathbf{3.4}$. Simulations with $\beta = 0.01$ and $\mathbf{Wi} = \mathbf{1}$.

taneous build-up of elastic normal stresses and their change in signs are responsible for the drop oscillations.

To observe the effect of a high Weissenberg number on the spread of the drop, simulations using $\mathbf{Re} = \mathbf{5}$, $\mathbf{Wi} = \mathbf{20}$ and $\beta = \mathbf{0.01}, \mathbf{0.1}, \mathbf{0.3}, \mathbf{0.5}, \mathbf{0.7}, \mathbf{0.9}, \mathbf{0.95}, \mathbf{0.99}$ were carried out. The evolutions of the diameter $d(t)$ obtained in these simulations are displayed in Fig. 9b for each value of β. It is seen that, after the drop has impacted the disk, the values of $d(t)$ corresponding to $\beta = \mathbf{0.3}, \mathbf{0.5}, \mathbf{0.7}, \mathbf{0.9}$ increased without any contraction, while the results corresponding to $\beta = \mathbf{0.95}, \mathbf{0.99}$ approached those of Newtonian flow, as expected. However, for $\beta = \mathbf{0.01}, \mathbf{0.1}$ the diameter $d(t)$ showed large expansions, that is, $d(t) > 2.5d_0$ for $\beta = 0.01$ and $d(t) > 2d_0$ at $\beta = \mathbf{0.1}$. For these two values of β the expansion of the drop was followed by its contraction to the value $d(t) \approx 0.044 = 2.2d_0$ for $\beta = 0.01$ and $d(t) \approx 0.04 = 2d_0$ for $\beta = \mathbf{0.1}$. Oscillations were not present at high **Wi** flow because the growth of the normal stresses are responsible for reversing the flow and subsequently they are dissipated. Those normal stresses also take longer to build-up and do not increase greatly because of the lower velocity gradients that appear after the impact.

To establish the validity of these results, we performed a mesh refinement analysis for the case $\mathbf{Re} = \mathbf{5}$, $\mathbf{Wi} = \mathbf{20}$ and $\beta = \mathbf{0.01}$. To demonstrate the convergence of the axisymmetric code on this flow, we employed the meshes **I, II, III, IV, V** that are defined in Table 7 and simulated the impacting drop from $t = 0$ to $t = 20$ on each of these meshes. The results obtained for the variation of $d(t)$ are displayed in Fig. 10 where it is seen that the results from mesh **I** approach to those of mesh **V** when the mesh is refined. This demonstrates the convergence of the axisymmetric code on this high Weissenberg number flow problem.

To better show the large deformations of the drop surface for $\mathbf{Re} = \mathbf{5}$, $\beta = \mathbf{0.01}$ and $\mathbf{Wi} = \mathbf{1}$ and **20**, Fig. 11 displays a three-dimensional view of the unsteady flow of the drop spreading over the disk at selected times. For $\mathbf{Wi} = \mathbf{1}$ (see the left column in the 3D visualizations), the drop initially expanded until $\mathbf{t} = \mathbf{2.6}$ and then contracted up to time $\mathbf{t} = \mathbf{3.1}$ when an elevation at the centre of the drop can be seen (see the associated 3D view). Subsequently, the drop again starts to expand, causing a depression at its centre at $\mathbf{t} \approx \mathbf{3.8}$. After this time the velocities within the drop are now small so that the drop surface does not show any substantial changes and gravity causes it to flow monotonically. We believe that these effects are due to elastic forces acting within the drop. These observations are in agreement with the time trace of the z-component of the velocity (w) shown in Fig. 12a that displays the velocities at the **cell(1,10)** located as shown in Fig. 7c. In particular, we observe that the w-velocity changes its sign several times, signalling the spreading and contracting phases.

The results at a higher $\mathbf{Wi} = \mathbf{20}$ are more dramatic. The high Weissenberg number means that it takes longer for the resisting polymer shear stresses to build-up after impact, so the drop was able to spread much more than at $\mathbf{Wi} = \mathbf{1}$; similarly, retraction took much longer to occur because the normal stresses take longer to relax to lower values,

Table 7
Meshes employed in the simulations of drop impacting with **Re = 5**, **Wi = 20** and $\beta = 0.01$.

Mesh spacing	I	II	III	IV	V
$(dr = dz)/d_0$	0.0166666	0.025000	0.0111111	0.0100000	0.0083333

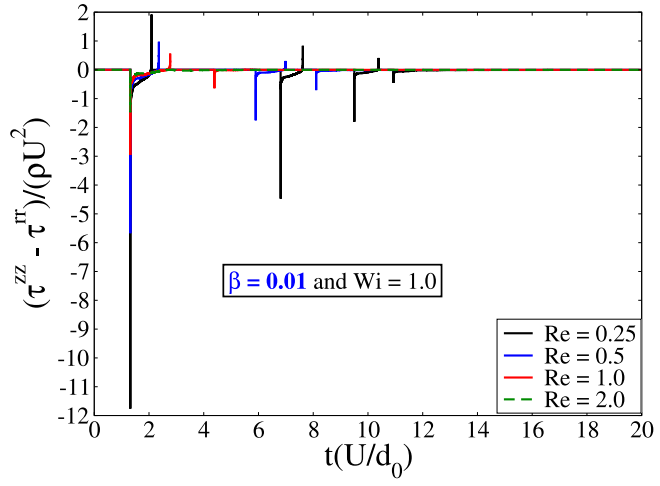

(a)

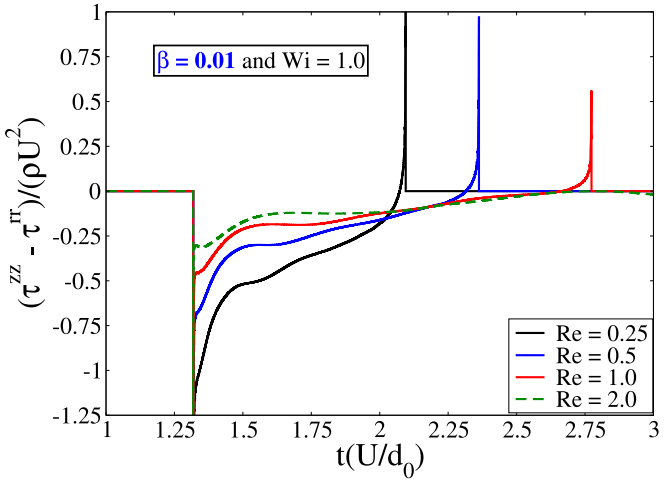

(b)

Fig. 16. (a) Variation of $N_1(t)$ at the cell(1,1) sketched in Fig. 7c for **Wi = 1**, $\beta = 0.01$ and several Reynolds numbers. (b) Zoom-in of the results in the region $[1,\ 3] \times [-1.25,\ 1]$. .

since they depend on smaller velocity gradients. The maximum spread took place at **t = 3.1** (see Fig. 11) where there are noticeable surface ripples. The thin layer of fluid at the perimeter of the disk would then appear to be affected by elastic forces causing the fluid to retract and move towards the centre; then, at **t = 5.7**, a small jet emerges at the centre of the drop. After that, a cycle of expansion and contraction continued, but was quickly attenuated due to viscous and gravity forces (see frames **t = 6.1, 7.6, 10.0**). Subsequently, there was little change in the shape of the drop as the fluid was almost quiescent (not shown). These observations are confirmed in Fig. 12b where the time variation of the velocities at **cell(1,10)** (identified in Fig. 7c) are displayed. Here we see that after **t = 8**, the velocities are very small resulting in little change in the shape of the surface of the drop.

Table 8
VALUES of **Re** and β employed in the simulation of bouncing drops.

Wi = 1					
$\beta = 0.01$ (**fixed**)	**Re**	**0.25**	**0.5**	**1.0**	**2.0**
Re = 0.25 (**fixed**)	β	**0.0**	**0.01**	**0.05**	**0.1**

4.4. Simulation of drop bouncing

In the drop impacting flow, when the amount of solvent is small, or the flow is highly elastic, the liquid droplet may rebound. This type of flow has attracted only a few computational rheologists. For instance, Xu et al. [27,30,31] applied their smoothed particle hydrodynamics (SPH) code to this problem using the **UCM** model in the absence of surface tension forces and were able to capture the drop bouncing.

In order to demonstrate that our numerical approach has the capability of modelling the drop bouncing phenomenon for the Oldroyd-B model, we performed several simulations with small values of the parameter β and, in addition we explored the conditions leading to such an event in the $\{\beta - \mathbf{Re} - \mathbf{Wi}\}$ phase space. The computational domain is the same as depicted in Fig. 7b. To verify if drop bouncing occurred, the time-dependence of the distance between the drop and the disk, **h(t)**, (see Fig. 7b) will be plotted. Thus, when the drop is attached to the disk, **h(t) = 0**, while if it rebounds, detaching itself from the disk, then **h(t)** will be positive. Eventually, due to the gravitational force, the drop will start to descend hitting the disk again (**h(t) = 0**,). It is anticipated that, depending on the values of β, **Re** and **Wi**, the drop may rebound several times, or even not at all.

To observe this effect, simulations were initially performed for several values of both the Reynolds number and the viscosity ratio given in Table 8, for a fixed Weissenberg number, **Wi = 1** and employing the mesh M4 defined in Table 6.

The flow conditions can be found in Table 5 with the exception of η_0 that was adjusted for the particular Reynolds number employed.

Fig. 13 displays a 3D-visualization of the fluid flow obtained with **Wi = 1** and $\beta = 0.01$ for **Re = 0.25, 0.5, 2.0**. **3D animation videos are provided in** Fig. 21 in the Appendix A.

At the time **t = 1.8**, the three drops have hit the disk and it can be seen that the Reynolds number has a substantial influence on both the velocity and shape of the drop. Indeed, for **Re = 0.25** and **0.5** the drop experiences a radial contraction (as is clear from the velocity field in Fig. 14), whereas at higher **Re** (**2.0**) the drop still spreads radially with a downwards vertical motion (see Fig. 14). These differences become more noticeable at time **t = 2.2** when it is seen that the drop with **Re = 0.25** has already bounced and is moving upwards against the gravitational field, whereas at **Re = 0.5, 2.0**, the drops are now undergoing contraction (i.e. fluid moving towards the centre). Finally, at time **t = 3.4**, the drops with **Re = 0.25** and **0.5** have rebounded and are moving upwards against gravity (see the velocity field in Fig. 14), whereas, the drop with **Re = 2.0** is seen to have partially left the ground while remaining partially attached (no rebound) and, is again spreading, as is clear from the velocity field in Fig. 14. The fact that the drop did not detach itself from the disk is likely to be due to the inertia force being stronger than the elastic forces.

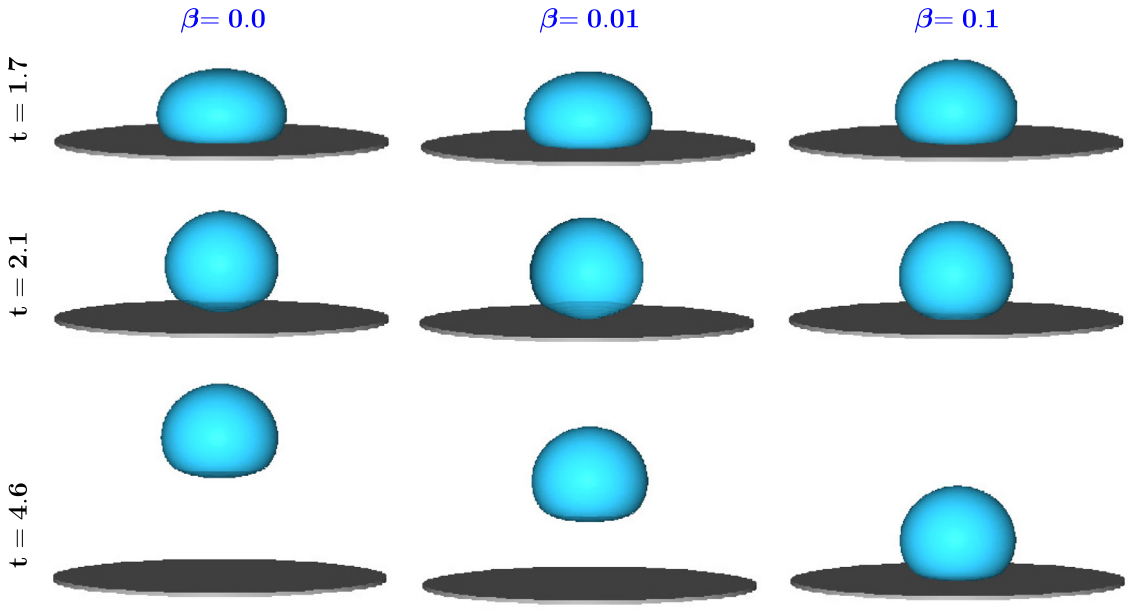

Fig. 17. Visualization of drop rebound at selected times for **Re** = **0.25**, **Wi** = **1** and several values of β.

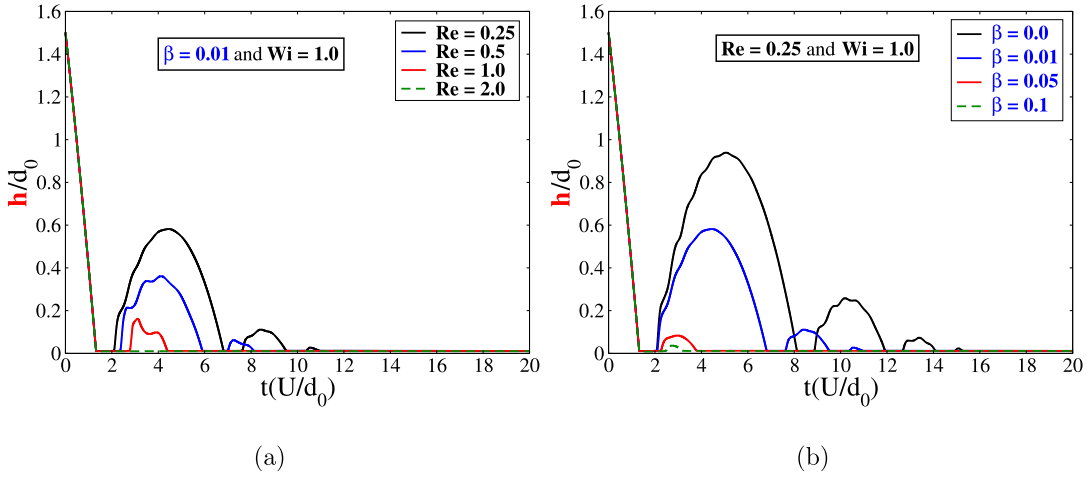

Fig. 18. Heights of bouncing drops for **Wi** = **1**: (a) $\beta = 0.01$ and varying **Re**, (b) **Re** = **0.25** varying the viscosity ratio β.

To provide additional insight into the phenomenon of the bouncing drop, Fig. 15 displays contours of the first normal stress difference $N_1(t) = \tau^{zz}(t) - \tau^{rr}(t)$ within the drop for **Re** = **0.25**, **0.5**, **2.0** at the times shown. It is seen that at the time **t** = **1.8** the three drops are attached to the disk and have high contour values for $N_1(t)$. However, at time **t** = **2.2** the drop with **Re** = **0.25** has already bounced and its values for $N_1(t)$ are relatively small. Drops with **Re** = **0.5** and **2.0** remain attached to the disk (i.e. do not bounce) and present reasonably high contour values for $N_1(t)$. At time **t** = **3.4** the drops with **Re** = **0.25** and **0.5** are bouncing upwards and giving rise to small contour values of $N_1(t)$ while the drop that has not bounced (**Re** = **2.0**) displays reasonable large contours of $N_1(t)$ throughout the drop. We point out that when the drops bounce, the first normal stress difference changes sign from negative to positive as displayed in Fig. 16a (a zoom in at the instant of time of bouncing is shown in Fig. 16b) and a region with positive countours of $N_1(t)$ builds up around the detachment point. This region then moves to the centre of the drop and changes its sign (as can be seen in Fig. 15).

Moreover, we see that at the time of impact at approximately **t** = **1.3** (see Fig. 16), the value of $N_1(t)$ decreases suddenly reaching large negative values (e.g. $N_1(t) \approx -11.8$ for **Re** = **0.25**, $N_1(t) \approx -5.5$ for **Re** = **0.5**, $N_1(t) \approx -2.5$ for **Re** = **1.0** and $N_1(t) \approx -1.5$ for **Re** = **2.0**). For instance, for **Re** = **0.25**, we can see in Fig. 16a that, prior to bouncing, $N_1(t)$ changes sign at **t** $\approx$ **2.1**, becoming positive and thereafter attaining a peak value of $N_1(t) \approx 2$. The occurrence of this peak value was due to the fact that the drop bounced and maintained an upward flow. Note that **cell(1,1)** does become empty over the time interval $\approx [2.1, 6.5]$ in which case all variables are set to zero explaining the discontinuity in Fig. 16a. The value of $N_1(t)$ that was plotted at the centre of **cell(1,1)** was thus zero until **t** $\approx$ **6.5** when the drop again impacts the disk and $N_1(t)$ attains another negative peak of $N_1 \approx -4.5$. During the time interval [2.1, 6.5], **h(t)** is positive and the drop is above the disk (see Fig. 18a). After the drop hits the disk at $t \approx 6.5$ the process is repeated: at **t** $\approx$ **7.5** the value of $N_1(t)$ becomes zero, the drop again bounces and the flow is vertically upwards until **t** $\approx$ **11.0** and so it continues. This process is repeated three times for **Re** = **0.25**, two times for **Re** = **0.5** and only once for **Re** = **1.0**. For **Re** = **2.0** the drop did not bounce as $h(t)$ was always zero (see Fig. 18a).

Fig. 17 displays the drop for a fixed **Re** = **0.25** and $\beta = 0.0, 0.01, 0.1$ at selected times. **3D animation videos are provided in** Fig. 22 **in the Appendix A.** This figure clearly shows that the drop-bouncing is associated with the polymer contribution to the total stress, with the **UCM** droplet exhibiting the greatest bounce. Increasing β, even to the

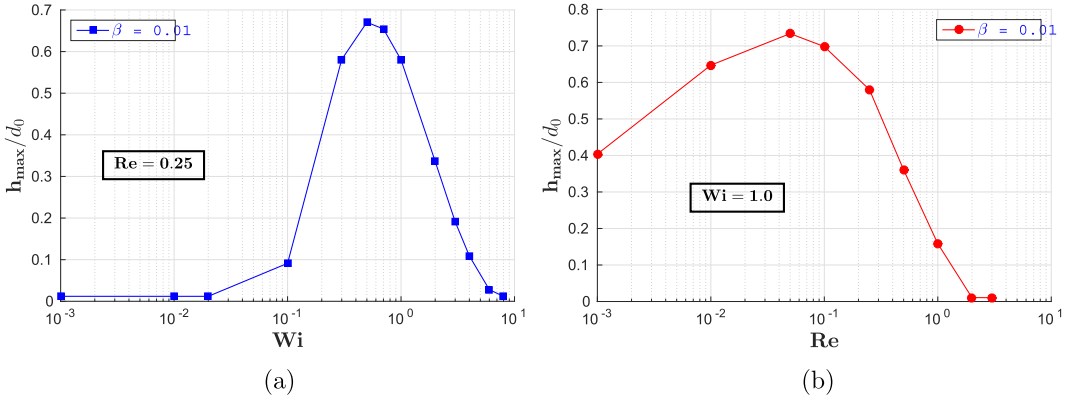

Fig. 19. Variation of the maximum height of h(t) as function of Weissenberg and Reynolds numbers.

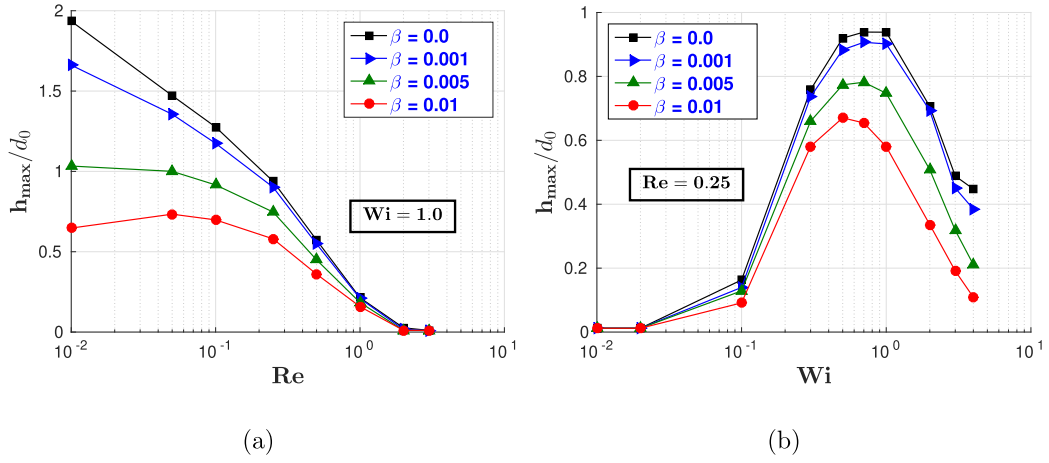

Fig. 20. Variation of the maximum height of h(t) as function of Reynolds and Weissenberg numbers. a) **Wi = 1** fixed, varying β and **Re**, b) **Re = 0.25** fixed, varying β and **Wi = 1**.

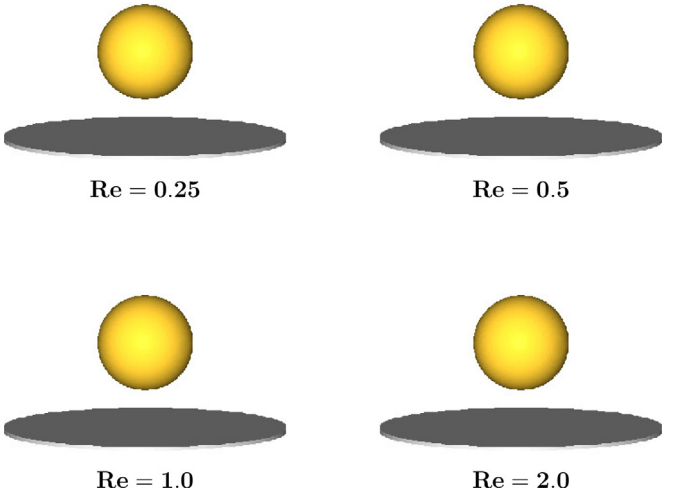

Fig. 21. Animations varying **Re**. Supplementary material shows animations of these flow conditions.

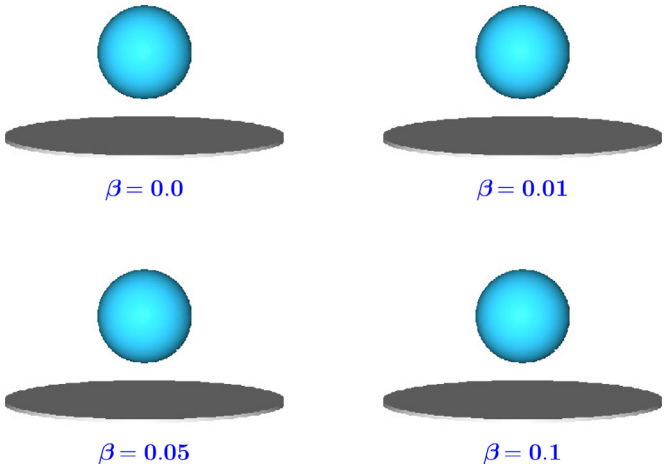

Fig. 22. Animations varying β. Supplementary material shows animations of these flow conditions.

small value of 0.01, has the effect of significantly reducing the height of the bouncing droplet. When the solvent viscosity contributes 10% to the total viscosity ($\beta = 0.1$) the droplet only bounces a small amount, but this is more clearly shown in Fig. 18. In Fig. 18, the variation of **h(t)** with time is displayed for several cases, at fixed **Wi = 1**, separately assessing the effects of **Re** and of β, complementing the previous figures.

It is clear that, the drops with $\beta = 0.0$ (**UCM** model) and $\beta = 0.01$ had a pronounced bounce, in some case bouncing more than once whereas the drop with $\beta = 0.1$ hardly bounced at all. For this particular **Re = 0.25** and **Wi = 1**, the first two solutions bounced three times with the height of their bounces decreasing with time as a direct result of potential energy loss (see Table 9). On the other hand, the drop with **Re = 1.0** displayed similar results, bouncing only once (see Fig. 18a and Table 9).

Table 9
VALUES of the maximum height $h(t)$ and associated time t_{max} of bouncing drops.

Wi = 1 and $\beta = 0.01$	Re	0.25	0.5	1.0	2.0
	$h(t)$	0.582	0.361	0.161	0.0
	t_{max}	4.450	4.121	3.116	
Wi=1 and **Re=0.25**	β	**0**	**0.01**	**0.05**	**0.1**
	$h(t)$	0.934	0.582	0.083	0.036
	t_{max}	5.058	4.450	2.966	2.737

Table 10
Weissenberg and Reynolds numbers employed in the simulation of the bouncing drop.

Variation of Wi	**Re=0.25** and $\beta = 0.01$ FIXED
Wi	0.001, 0.01, 0.02, 0.1, 0.3, 0.5, 0.7, 1.0, 2.0, 3.0, 4.0, 6.0, 8.0
Variation of **Re**	**Wi=1** and $\beta = 0.01$ FIXED
Re	0.001, 0.01, 0.05, 0.1, 0.25, 0.5, 1.0, 2.0, 3.0

Table 11
Simulation of bouncing drops varying β, **Re** and *Wi*.

Wi=1, FIXED	
β	**0.0, 0.001, 0.005, 0.01**
Re	0.01, 0.05, 0.1, 0.25, 0.5, 1.0, 2.0, 3.0
$Re = 0.25$, FIXED	
β	**0.0, 0.001, 0.005, 0.01**
Wi	0.01, 0.02, 0.1, 0.3, 0.5, 0.7, 1.0, 2.0, 3.0, 4.0

4.4.1. Limiting Weissenberg and Reynolds numbers

To examine the effect of the Weissenberg and Reynolds numbers on the bouncing of droplets, a number of simulations were performed using the values of **Wi** and **Re** displayed in Table 10. In particular, we are interested in investigating the effects of **Wi** and **Re** on the maximum height of the drop ($\mathbf{h_{max}}$), which takes place after the drops first rebound. (Note that it may rebound several times as can be seen in the videos provided in Figs. 21 and 22). We are also interested in determining the range of Weissenberg and Reynolds numbers for which bouncing occurs.

The values of the maximum heights ($\mathbf{h_{max}}$) obtained in these simulations are plotted in Fig. 19. It can be seen in Fig. 19a that the Weissenberg number has a significant influence on the degree of bouncing. For the values of **Re** and β employed in these simulations, the drops rebound if the Weissenberg number lies in the interval $[0.02, 8.0]$; the maximum height was attained when $\mathbf{Wi = 0.5}$. The reason that the drop did not rebound for smaller values of **Wi** is because in this case the flow is approaching Newtonian flow and elasticity effects are small; however, if **Wi** is sufficiently large (**Wi= 8**), even though the drop is very elastic, the elastic stress build-up after hitting the solid surface is too long and the spreading of the droplet dissipates too much energy in the meantime and consequently the drop does not rebound.

The results, obtained varying the Reynolds number, are displayed in Fig. 19b where it is observed that the Reynolds number also strongly affects the bouncing. If **Re** increases then the maximum height of the drop starts to decrease and if **Re** is sufficiently large ($\mathbf{Re = 2}$) then bouncing does not occur because of excessive inertia. On the other hand, if **Re** decreases then the height of the bounce decreases (at least for the Reynolds numbers simulated).

To investigate the effect of β on the maximum height of the bounce when **Re** and **Wi** are varied, we performed additional simulations using the values of β, **Re** and **Wi** displayed in Table 11. Fig. 20a displays the maximum heights obtained for the values of β and **Re** simulated. Again it is seen that when the Reynolds number increases, the maximum height of the bounce decreases to zero, meaning that the drop ceases to bounce at sufficiently large Reynolds number. This is in accordance with the fact that increasing the inertia causes the drop to spread more radially loosing energy due to the action of viscosity and therefore the drop bounces less, eventually not bouncing at all. The results obtained with variation of the Weissenberg number are displayed in Fig. 20b. It is seen that for small values of **Wi** the maximum height of the bounce decreases to zero due to the fact that the drop begins to behave like a Newtonian fluid. When $\mathbf{Wi > 1}$ the maximum height decreases because the ratio between the characteristic time of the fluid and the characteristic time of the flow increases.

The decrease in the value of β, that is as the UCM fluid is approached, makes the drop more elastic so bouncing is more pronounced.

5. Conclusions

This work presented a novel numerical algorithm for solving time-dependent free surface flows of Oldroyd-B fluids which is stable for the whole range of the ratio of solvent to total viscosity. The formulation employed to solve the governing equations and the free surface stress conditions made use of an EVSS transformation. This approach removed the multiplicative factor $\mathbf{1}/\beta$ from the components of the zero stress conditions on the free surface, and the inevitable numerical instabilities that do ensue when the fluid approached the **UCM** limit.

A crucial feature of the method was how the Oldroyd-B constitutive equation was solved. The extra-stress tensor was written in terms of the conformation tensor **A** which was approximated by implicit finite differences resulting in a (4×4)-linear system that was solved exactly. After obtaining the conformation tensor the extra-stress tensor was easily directly evaluated. The method was verified against fully developed pipe flow for an Oldroyd-B fluid and convergence results were provided. The efficacy of this new methodology for unsteady free surface flow was demonstrated by simulating the impacting drop problem; here mesh refinement was performed, with particular focus on vanishingly small values of viscosity ratio, β. The subsequent, more extensive, investigation using the Oldroyd-B model assessed the effects of the viscosity ratio, Reynolds number and Weissenberg number on the height of bouncing droplets. In particular, we found that the solvent contribution, represented by the value of β, had a substantial influence on the height of the bouncing drop. How the Reynolds and Weissenberg numbers affect the height of the bounce was also discussed at length.

Declaration of Competing Interest

The authors declare that they have no known competing financial interests or personal relationships that could have appeared to influence the work reported in this paper.

Acknowledgments

The authors would like to acknowledge the financial support given by the funding agencies: CNPq - Conselho Nacional de Desenvolvimento Científico e Tecnológico Grant No. 305405/2018-7, FAPESP Grant No. 2013/07375-0 (CEPID-CeMEAI project) and CAPES Grant No. PROEX-9259544/D. The fourth author would like to acknowledge a travel grant from the Edinburgh Mathematical Society. F. T. Pinho acknowledges funding from Fundação para a Ciência e a Tecnologia through projects UIDB/00532/2020, and PTDC/EMS-ENE/2390/2014, POCI-01-0145-FEDER-016669.

Appendix A. The videos must be downloaded from the Supplementary Material

Supplementary material

Supplementary material associated with this article can be found, in the online version, at doi:10.1016/j.jnnfm.2020.104338

References

[1] R.G. Owens, T.N. Phillips, Computational Rheology, Imperial College Press, 2002. ISBN 978-1-86094-186-3

[2] J.C. Oldroyd, On the formulation of rheological equations of state, Proceed. Roy. Soc. Lond. Ser. A, Math. Phys. Sci. **200** (1950) 523–541.

[3] N. Phan-Thien, R.I. Tanner, A new constitutive equation derived from network theory, J. Non Newtonian Fluid Mech. **2** (1977) 353–365.

[4] H. Giesekus, A simple constitutive equation for polymer fluids based on the concept of deformation-dependent tensorial mobility, J. Non Newtonian Fluid Mech. **11** (1982) 69–109.

[5] R.B. Bird, R.C. Armstrong, O. Hassager, Dynamics of Polymeric Liquids, **2**, Wiley, New York, 1987.

[6] T.C.B. McLeish, R.G. Larson, Molecular constitutive equations for a class of branched polymers: the pom-pom polymer, J. Rheol. **42** (1998) 81–110.

[7] W.M.H. Verbeeten, G.W.M. Peters, F.P.T. Baaijens, Differential constitutive equations for polymer melts: the extended pom-pom model, J. Rheol. **45** (2001) 823–843.

[8] A.C. Papanastasiou, L.E. Scriven, C.W. Macso, An integral constitutive equation for mixed flows: viscoelastic characterization, J. Rheol. **27** (1983) 387–410.

[9] A. Kaye, Non-Newtonian Flow in Incompressible Fluids, note no. 134, College of Aeronautics, Cranfield, UK, 1962.

[10] X.L. Luo, E. Mitsoulis, An efficient algorithm for strain history tracking in finite element computations of non-newtonian fluids with integral constitutive equations, Int J Numer Methods Fluids **11** (1990) 1015–1031.

[11] M.J. Crochet, R. Keunings, Die swell of a maxwell fluid: numerical prediction, J. Non Newtonian Fluid Mech. **7** (1980) 199–212.

[12] M.J. Crochet, R. Keunings, Finite element analysis of die swell of a highly elastic fluid, J. Non Newtonian Fluid Mech. **10** (1982) 339–356.

[13] V. Delvaux, M.J. Crochet, Numerical simulation of delayed die swell, Rheol. Acta **29** (1990) 1–10.

[14] M.F. Tomé, N. Mangiavacchi, J.A. Cuminato, A. Castelo, S. McKee, A finite difference technique for simulating unsteady viscoelastic free surface flows, J. Non Newtonian Fluid Mech. **106** (2002) 61–106.

[15] A. Bonito, M. Picasso, M. Laso, Numerical simulation of 3d viscoelastic flows with free surfaces, J. Comput. Phys. **215** (2006) 691–716.

[16] M.F. Tomé, L. Grossi, A. Castelo, J.A. Cuminato, S. McKee, K. Walters, Die-swell, splashing drop and a numerical technique for solving the oldroyd b model for axisymmetric free surface flows, J. Non Newtonian Fluid Mech. **141** (2007) 148–166.

[17] M.F. Tomé, A. Castelo, J. Murakami, J.A. Cuminato, R. Minghin, M.C.F. Oliveira, N. Mangiavacchi, S. McKee, Numerical simulation of axisymmetric free surface flows, J. Comput. Phys. **157** (2000) 441–472.

[18] D. Rajagopalan, R.C. Armstrong, R.A. Brown, Finite element methods for calculation of steady viscoelastic flow using constitutive equations with a newtonian viscosity, J. Non Newtonian Fluid Mech **36** (1990) 159–192.

[19] R. Guénette, M. Fortin, A new mixed finite element method for computing viscoelastic flows, J. Non Newtonian Fluid Mech. **60** (1995) 27–52.

[20] H. Matallah, P. Townsend, M.F. Webster, Recovery and stress-splitting schemes for viscoelastic flows, J. Non Newtonian Fluid Mech. **75** (1998) 139–166.

[21] L.J. Amoreira, P.J. Oliveira, Comparison of different formulations for the numerical calculation of unsteady incompressible viscoelastic fluid flow, Adv. Appl. Math. Mech. **2** (2010) 483–502.

[22] G.K. Batchelor, An Introduction of Fluid Dynamics, Cambridge University Press, Cambridge, 1967.

[23] M.F. Tomé, A. Castelo, V.G. Ferreira, S. McKee, A finite difference technique for solving the oldroyd-b model for 3d-unsteady free surface flows, J. Non Newtonian Fluid Mech. **154** (2008) 179–206.

[24] J. Peng, K.Q. Zhu, Instability of the interface in co-extrusion flow of two UCM fluids in the presence of surfactant, J. Non Newtonian Fluid Mech. **166** (2011) 152–163.

[25] D. Izbassarov, M. Muradoglu, A front-tracking method for computational modeling of viscoelastic two-phase flow systems, J. Non Newtonian Fluid Mech. **223** (2015) 122–140.

[26] R.A. Figueiredo, C.M. Oishi, J.A. Cuminato, J.C. Azevedo, A.M. Afonso, M.A. Alves, Numerical Investigation of Three Dimensional Viscoelastic Free Surface Flows: Impacting Drop Problem, in: E. Onate, J. Oliver, A. Huerta (Eds.), Proceedings of 6th European Conference on Computational Fluid Dynamics (ECFD VI), Barcelona, Spain, 2014.

[27] X. Xu, J. Ouyang, T. Jiang, Q. Li, Numerical simulation of 3d-unsteady viscoelastic free surface flows by improved smoothed particle hydrodynamics method, J. Non Newtonian Fluid Mech. **177–178** (2012) 109–120.

[28] H. Jasak, A. Jemcov, Z. Tukovic, OpenFOAM: a c++ library for complex physics simulations, Int. Worksh. Coupl. Method. Num. Dyn. IUC Dubrovnik, Croatia (2007) 1–20.

[29] E. Castillo, J. Baiges, R. Codina, Approximation of the two-fluid flow problem for viscoelastic flows using the level set method and pressure enriched finite element functions, J. Non Newtonian Fluid Mech. **225** (2015) 37–53.

[30] X. Xu, X.L. Deng, An improved weakly compressible SPH method for simulating free surface flows of viscous and viscoelastic fluids, Comput. Phys. Commun. **201** (2016) 43–62.

[31] X. Xu, P. Yu, A technique to remove the tensile instability in weakly compressible SPH, Comput. Mech. **39** (2018) 1–18.

[32] R. Comminal, F. Pimenta, J.H. Hattel, M.A. Alves, J. Spangenberg, Numerical simulation of the planar extrudate swell of pseudplastic and viscoelastic fluids with the streamfunction and the VOF methods, J. Non Newtonian Fluid Mech. **252** (2018) 1–18.

[33] R. Fattal, R. Kupferman, Time-dependent simulation of viscoelastic flows at high weissenberg number using the log-conformation representation, J. Non Newtonian Fluid Mech. **126** (2005) 23–37.

[34] K. Walters, M. Webster, The distinctive CFD challenges of computational rheology, Int. J. Numer. Method. Fluid. **43** (2003) 577–596.

[35] C.W. Hirt, B.D. Nichols, Volume of fluid (VOF) method for the dynamics of free boundaries, J. Comput. Phys. **39** (1981) 201–225.

[36] M.S. Kim, W.I. Lee, A new VOF-based numerical scheme for the simulation of fluid flow with free surface. part i: new free surface-tracking algorithm and its verification, Int. J. Numer. Method. Fluid. **42** (2003) 765–790.

[37] C.F. JanBen, S.T. Grilli, M. Krafczyk, On enhanced non-linear free surface flow simulations with a hybrid LBM-VOF model, Comput. Math. Applic. **65** (2013) 211–229.

[38] Q. Zhang, On a family of unsplit advection algorithms for volume-of-fluid methods, SIAM J. Numer. Anal. **51** (2013) 2822–2850.

[39] N.O. Moraga, L.A. Lemus, M.A. Saavedra, R.A. Lemus-Mondaca, VOF/FVM Prediction and experimental validation for shear-thinning fluid column collapse, Comput. Math. Applic. **69** (2015) 89–100.

[40] R.A. Figueiredo, C.M. Oishi, A.M. Afonso, I.V.M. Tasso, J.A. Cuminato, A two-phase solver for complex fluids: studies of the weissenberg effect, Int. J. Multiphase Flow **84** (2016) 98–115.

[41] S. Osher, J.A. Sethian, Fronts propagating with curvature-dependent speed: algorithms based on hamilton-jacobi formulations, J. Comput. Phys. **79** (1988) 12–49.

[42] D. Deganello, A.J. Williams, T.N. Croft, A.S. Lubansky, D.T. Gethin, T.C. Claypole, Level-set method for the modelling of liquid bridge formation and break-up, Comput. Fluid. **40** (2011) 42–51.

[43] L. Ville, L. Silva, T. Coupez, Convected level set method for the numerical simulation of fluid buckling, Int. J. Numer. Method. Fluid. **66** (2011) 324–344.

[44] X. Zhuang, J. Ouyang, W. Li, Y. Li, Three-dimensional simulations of non-isothermal transient flow and flow-induced stresses during the viscoelastic fluid filling process, Int. J. Heat Mass Transf. **104** (2017) 374–391.

[45] S. Osher, R.P. Fedkiw, Level set methods: an overview and some recent results, J. Comput. Phys. **169** (2001) 463–502.

[46] M. Sussman, P. Smereka, S.J. Osher, A level set approach to computing solutions to incompressible two-phase flow, J. Comput. Phys. **114** (1994) 14–159.

[47] H. Kohno, T. Tanahashi, Numerical analysis of moving interfaces using a level set method coupled with adaptive mesh refinement, Int. J. Numer. Method. Fluid. **45** (2004) 921–944.

[48] J.A. Sethian, Evolution, implementation, and application of level set and fast marching methods for advancing fronts, J. Comput. Phys. **169** (2001) 503–555.

[49] H.-S. Dou, B.C. Khoo, N. Phan-Thien, K.S. Yeo, R. Zheng, Simulations of fibre orientation in dilute suspensions with front moving in the filling process of a rectangular channel using level-set method, Rheol. Acta **46** (2007) 427–447.

[50] F.H. Harlow, J.E. Welch, Numerical calculation of time-dependent viscous incompressible flow of fluid with free surface, Phys. Fluid. **8** (1965) 2182–2189.

[51] M.F. Tomé, J. Bertoco, C.M. Oishi, M.S.B. Araujo, D. Cruz, F.T. Pinho, M. Vynnycky, A finite difference technique for solving a time strain separable k-BKZ constitutive equation for two-dimensional moving free surface flows, J. Comput. Phys. **311** (2016) 114–141.

[52] A.A. Amsden, F.H. Harlow, A simplified MAC technique for incompressible fluid flow calculations, J. Comput. Phys. **6** (1970) 322–325.

[53] G. Tryggvason, B. Bunner, A. Esmaeeli, D. Juric, N. Al-Rawahi, W. Tauber, J. Han, S. Nas, Y.J. Jan, A front-tracking method for the computations of multiphase flows, J. Comput. Phys. **169** (2001) 70–759.

[54] M. Irfan, M. Muradoglu, A front tracking method for direct numerical simulation of evaporation process in a multiphase system, J. Comput. Phys. **337** (2017) 132–153.

[55] M.R. Pivello, M.M. Villar, R. Serfaty, A.M. Roma, A. Silveira-Neto, A fully adaptive front tracking method for the simulation of two phase flows, Int. J. Multiph. Flow **58** (2014) 72–82.

[56] M. Muradoglu, S. Tasoglu, A front-tracking method for computational modeling of impact and spreading of viscous droplets on solid walls, Comput. Fluid. **39** (2010) 615–625.

[57] Y. Wang, M. Do-Quang, G. Amberg, Impact of viscoelastic droplets, J. Non Newtonian Fluid Mech. **243** (2017) 38–46.

[58] W. Yi, D. Corbett, X.F. Yuan, A sharp-interface cartesian grid method for viscoelastic fluid flow in complex geometry, J. Non Newtonian Fluid Mech. **234** (2016) 82–104.

[59] H. Terashima, G. Tryggvason, A front-tracking/ghost-fluid method for fluid interfaces in compressible flows, J. Comput. Phys. **228** (2009) 4012–4037.

[60] M.F. Tomé, A. Castelo, A.M. Afonso, M.A. Alves, F.T. Pinho, Application of the log–conformation tensor to three-dimensional time-dependent free surface flows, J. Non Newtonian Fluid Mech. **175–176** (2012) 44–54.

[61] A.J. Chorin, Numerical solution of the navier-stokes equations, Math. Comput. **22** (1968) 745–762.

[62] M.F. Tomé, B. Duffy, S. McKee, A numerical technique for solving unsteady non-newtonian free surface flows, J. Non Newtonian Fluid Mech. **62** (1996) 9–34.

[63] C.M. Oishi, M.F. Tomé, J.A. Cuminato, S. McKee, An implicit technique for solving 3d low reynolds number moving free surface flows, J. Comput. Phys. **227** (2008) 7446–7468.

[64] M.A. Alves, P. Oliveira, F.T. Pinho, A convergent and universally bounded interpolation scheme for the treatment of advection, Int. J. Numer. Method. Fluid. **41** (2003) 47–75.